Simulating Preferential Flow by A Multi-dimensional Process-based HYDRUS Model

Ying Zhao[1], Yi Jun[2], Rongjiang Yao[3], Fei Li[4], and Robert Lee Hill[5]

[1]Ludong University
[2]Central China Normal University
[3]Chinese Academy of Sciences
[4]Chinese Academy of Agricultural Sciences
[5]University of Maryland

November 23, 2022

Abstract

Preferential flow processes are controlled by subsurface structures with the hierarchical organization across scales, but there is a lack of multiscale model validation using the field data. In this study, using a comprehensive dataset collected in the forested Shale Hills catchment, we tested and validated preferential flow occurrence by 2-dimension HYDRUS-2D at the hillslope scale, and in comparison, with 1-dimension HYDRUS-1D at the pedon scale and 3-dimension HYDRUS-3D at the catchment scale. There was good agreement between the 1D simulations and measurements of soil moisture in the soil profile, which was mainly affected by the vertical change in porosity/permeability with depth and precipitation characteristics; however, short-term fluctuations due to preferential flow were poorly captured. Notably, 2D and 3D simulations, accounting for preferential flow controlled by slope positions and shallow fractured bedrock, provided better results than the 1D simulations. Furthermore, a dual-porosity or anisotropic model provided more accurate predictions of soil moisture than a single-porosity or isotropic model due to a more realistic representation of local soil and fractured shale structure, which is also the premise of preferential flow (PF) occurrence. Consequently, our study reflected the central importance of multi-dimensional model approaches while highlighting the quantification of the soil structure and fractured nature of the bedrocks itself is essential to the simulation of preferential flow. The multi-dimensional modeling approaches can provide the mechanic presentation of PF pathways to the first-order stream and the necessity of the 3D simulation with detailed information to identify the dominant hydrological process.

Simulating Preferential Flow by A Multi-dimensional Process-based HYDRUS Model

Ying Zhao[1,2,*], Jun Yi[3], Rongjiang Yao[4], Fei Li[5], Robert Lee Hill[6]

[1]College of Resources and Environmental Engineering, Ludong University, Yantai 264025, China; [2]Global Institute for Water Security, University of Saskatchewan, Saskatoon, Saskatchewan, Canada; [3]Hubei Province Key Laboratory for Geographical Process Analysis and Simulation, Central China Normal University, Wuhan 430079, China; [4]State Key Laboratory of Soil and Sustainable Agriculture, Institute of Soil Science, Chinese Academy of Sciences, Nanjing 210008, China; [5]Grassland Research Institute, Chinese Academy of Agricultural Sciences, Huhhot 010010, China; [6]Department of Environmental Science and Technology, University of Maryland, College Park, MD 20742, USA.

[*]Corresponding author: yzhaosoils@gmail.com (Y. Zhao)

Abstract: Preferential flow processes are controlled by subsurface structures with the hierarchical organization across scales, but there is a lack of multiscale model validation using the field data. In this study, using a comprehensive dataset collected in the forested Shale Hills catchment, we tested and validated preferential flow occurrence by 2-dimension HYDRUS-2D at the hillslope scale, and in comparison, with 1-dimension HYDRUS-1D at the pedon scale and 3-dimension HYDRUS-3D at the catchment scale. There was good agreement between the 1D simulations and measurements of soil moisture in the soil profile, which was mainly affected by the vertical change in porosity/permeability with depth and precipitation characteristics; however, short-term fluctuations due to preferential flow were poorly captured. Notably, 2D and 3D simulations, accounting for preferential flow controlled by slope positions and shallow fractured bedrock, provided better results than the 1D simulations. Furthermore, a dual-porosity or anisotropic model provided more accurate predictions of soil moisture than a single-porosity or isotropic model due to a more realistic representation of local soil and fractured shale structure, which is also the premise of preferential flow (PF) occurrence. Consequently, our study reflected the central importance of multi-dimensional model approaches while highlighting the quantification of the soil structure and fractured nature of the bedrocks itself is essential to the simulation of preferential flow. The multi-dimensional modeling approaches can provide the mechanic presentation of PF pathways to the first-order stream and the necessity of the 3D simulation with detailed information to identify the dominant hydrological process.

Keywords: Hydrological processes; Preferential flow; Multi-dimensional Model; Fracture bedrock; HYDRUS

34 Soil is a three-dimensional structural unit affected by preferential flow processes under
35 varying precipitation inputs, soil-terrain attributes, and moisture conditions. Preferential flow
36 (PF), defined by Hendrickx and Flury (2001) as 'all phenomena where water and solutes
37 move along certain pathways, while bypassing a fraction of the porous matrix', results in
38 irregular wetting patterns in which water move faster in certain parts of the soil profile than in
39 others (Freeze, 1972). Understanding the dynamics of PF is critical for explaining water flow
40 through soils, the design of monitoring schemes, and for formulating models (Lin and Zhou,
41 2008; Clark et al., 2015). In the early periods, hydrology was considered one-dimensional
42 and neglected the three-dimensional (3D; vertical + lateral) subsurface water flow (Fan et al.,
43 2019). It is necessary to include PF phenomena such as fast transport through macropores,
44 furrow flow due to the spatial variability of hydraulic properties, and fingering flow due to
45 the instability of wetting fronts (Vogel and Roth, 2003; Vereecken et al., 2015; Gao et al.,
46 2018).

47

48 Although PF is ubiquitous in hydrology, its proper identification and representation in
49 hydrological models remain a challenge (Schulz et al., 2006; Beven and Germann, 2013;
50 Clark et al., 2015; Gu et al., 2018). The PF and their subsequent processes are intimately
51 related to the spatial structure of the subsurface heterogeneities caused by biologic or
52 geological activities and geomorphological and soil-forming processes (Beven and Germann,
53 1982; Nimmo, 2012; Beven and Germann, 2013; Liu and Lin, 2015). This often presents over
54 a hierarchy of scales and affect PF from the soil pedon up to the catchment scale (Blöschl and
55 Grayson, 2001; McDonnell et al., 2007; Korres et al., 2015). In general, three distinctive
56 scales are recognized. They are represented by three different conceptual and physical models
57 for water flow in the vadose zone: pore scale, Darcian scale, and catchment scale (Hendrickx
58 and Flury, 2001). A typical pore-scale PF is saturated, and unsaturated water flows through
59 macropores and fractures. At the Darcian scale, unstable flow occurs in water repellent soils
60 and layered soil profiles, and PF can also be induced by variability in soil hydraulic
61 properties. At the areal scale, surface depressions and discontinuous layers with lower or
62 higher permeabilities can cause PF. When multiple spatial scales are involved, the features at
63 a smaller scale often form boundary conditions for the processes acting at a larger scale
64 (Bittelli et al., 2010).

65

66 Up to now, the scales of spatial simulation models are usually too large to include the effects
67 of lateral flow on soil water (Fan et al., 2019). Whatever the representative area of a model

68 domain is, the critical issue is whether the model code can define the complex but truly
69 pedological and hydrological processes, assuming similar media scaling theory. Several
70 studies have been conducted to compare various codes and approaches describing
71 equilibrium water flow in the vadose zone (e.g., Scanlon et al., 2002), similar comparisons
72 simulating preferential and nonequilibrium flow are lacking (Larsson and Jarvis, 1999).
73 Especially, few models have developed to quantify those effects of heterogeneity and
74 topography combined with scaling issues on hydrological fluxes (Ebel et al., 2007; Bittelli et
75 al., 2010; Clark et al., 2015). Modelers generally rely on plot-scaled physical descriptions of
76 water flow to describe the hillslope scale water balance (Tromp-van Meerveld and Weiler,
77 2008). Comparisons of 2D and 3D simulations of lateral convergence flow have shown that
78 3D simulation provides significantly better results (Loague et al., 2006; Mirus et al., 2007;
79 Fan et al., 2019).

80

81 Another challenge of hydrological models is assessing various uncertainties, such as
82 expressions of soil and bedrock features and boundary conditions (Loos et al., 2007). While
83 previous research has mostly concentrated on uniform water flow with a single-porosity
84 model, many experiments have demonstrated the presence of nonequilibrium flow with dual-
85 porosity models (Beven and Germann, 1982; Durner, 1994; Šimůnek et al., 2006). For
86 instance, laterally oriented macropore flow may dominate in areas where the macropores are
87 created by plant roots (Newman et al., 1998; Gao et al., 2018). Especially in models of water
88 movement in complex landscapes, lateral flow due to differences either in anisotropic
89 hydraulic conductivity or topography should be taken into account (Buttle and McDonald,
90 2002; Maxwell and Kollet, 2008). Besides, lateral flow occurring at the interface between soil
91 and bedrock and/or at the soil and hydrologically-impeding layers such as fragipans, has been
92 recognized as an essential contributor to hillslope flow paths (e.g., Freer et al., 1997; Haga et
93 al., 2005; Fan et al., 2019). However, only a few models have included a permeable soil-
94 bedrock interface, and even fewer have tested this assumption with measurement data (Todd
95 et al., 2000; Ebel et al., 2007; Camporese et al., 2019). Using some virtual experiments with a
96 3D physics-based model, Hopp and McDonnell (2009) systematically investigated the
97 interactions between some of the dominant controls on subsurface stormflow generation.
98 However, their model still lacked predictions of PF that could have been validated with actual
99 measurements.

100

101 To clarify the extent and processes of PF, we investigated a forested Shale Hills watershed,
102 characterized by the available high temporal and spatial resolution of soil moisture
103 measurements. Previous studies at this critical zone observation site showed that the various
104 landscape elements differ significantly in soil texture and structure with no systematic trend
105 (Lin and Zhou, 2008; Guo et al., 2014), and PF was frequent (Zhao et al., 2012; Liu et al.,
106 2015). We postulate that incorporating different soil types and their detailed spatial
107 distributions into a physically-based model will enhance understanding of water flow
108 mechanisms and predictability of PF. For this reason, we employed the Richards equation-
109 based numerical model HYDRUS (Šimůnek et al., 2006), which includes a hierarchical
110 system of various approaches simulating PF in the vadose zone. HYDRUS is well tested and
111 widely used in diverse applications (Scanlon et al., 2002; Kohne et al., 2004; Saito et al.,
112 2006; Twarakavi et al., 2008; Šimůnek et al., 2016). One of the remaining questions is
113 whether this small-scale physics-based model, fed with accurate data, can adequately
114 simulate the behavior of complex hydrological systems (e.g., PF) at a relatively large scale
115 (Vereecken et al., 2015). In contrast, the previous larger-scale high-resolution models are still
116 far from capturing the impacts of hillslope-scale structures on PF (Fan et al., 2019). Another
117 similar question is how much complexity of dimension is needed in hydrological models,
118 particularly in terms of conceptual clarity and computational efficiency (Tromp-van
119 Meerveld and Weiler, 2008). Fan et al. (2019) considered that, in contrast to the 1-D, few-
120 meters deep, and free-draining soil hydrology in most earth system models, 3-D, lateral ridge-
121 to-alley flow through shallow and deep paths is the top globally quantifiable organizers of
122 water and energy (and vegetation) within a model domain.

123

124 In this study, we focus our attention on examining the influence of spatial scale, soil porosity
125 and anisotropy, and bedrock permeability on the development of PF. Our objectives are: (1)
126 to assess the capabilities of multi-dimensional modeling in identifying the critical processes
127 and parameters governing PF, (2) to evaluate the ability of the dual-porosity and anisotropic
128 models to describe mechanisms of PF, and (3) to elucidate how soil-bedrock conditions affect
129 PF occurrence from top-ridge to the first-order stream. The elements have been well tested
130 individually but not previously applied in such an integrated manner for water resources or
131 environmental modeling applications.

132

133 ## Materials and Methods

134

Experimental Site and Measurements

The model simulations presented here were based on field monitoring carried out at a 7.9-ha forested Shale Hills catchment, situated in central Pennsylvania, USA (Fig. 1), for four years from 2007 to 2010. Soil moisture monitoring indicated the existence of PF, which was influenced by soil properties such as soil type, soil depth, permeability, and soil location.

Experimental Site

The Shale Hills catchment has a typical humid continental climate, with a minimum mean monthly temperature of –3°C in January, a maximum mean monthly temperature of 22°C in July, and annual precipitation of about 980 mm (National Weather Service, State College, PA). The V-shaped catchment is drained by a first-order stream in the valley and has moderately steep slopes of up to 25–48% on both sides of the stream. Elevation ranges from 256 m at the outlet of the catchment to 310 m at the highest ridge. The catchment is underlain by about 300-m thick, steeply bedded, highly fractured Rose Hill Shale, and covered by maple-oak-hickory forest. The soils have a silt loam and silty clay loam texture, which were formed from shale colluvium or residuum, with many channel shale fragments throughout most of the soil profiles (Table 1).

Field monitoring

For the in-situ monitoring, sensors were installed at four sites (Figure 1, Table 1), which characterized by the four soil series: Weikert series on a hilltop (Site 74), Berks series at a mid-slope (Site 53), Rushtown series at the downslope of a swale (Site 51), and Blairton series close to the first-order stream that is at the outlet of a swale (Site 15). An array of sensors was installed at each site to measure soil water content, soil matrix potential, and soil temperature by soil horizons. For the PF analysis, this paper mainly focused on the soil moisture data obtained at 10-minute intervals using the ECH_2O probes (Decagon Devices, Inc., Pullman, WA) with an accuracy of ±3% and a measurement resolution of 0.1%. Our previous reports had identified a PF to occur when a subsurface soil horizon responded to a rainfall input earlier than a soil horizon above it (Lin and Zhou, 2008). Here we take the monitoring data we also used for the model test as an example. Figure 2 shows that the underlying R horizon responses to the storm events while overlying soil horizons did not respond at site 74 near the hilltop. At site 51 in the middle of a swale, a rapid 2.0% increase in soil moisture was apparent at 0.18- and 0.25-m depths in the B horizon, while soil moisture in the horizons above and below the B horizon did not change similarly. Intuitively, when a

167 soil moisture sensor buried in a subsoil responded to a storm event earlier than other sensors
168 above it, the water likely bypassed the overlying horizon(s) (i.e., vertical PF) or had
169 infiltrated into the deeper subsoil from the upslope or side-slope areas (i.e., lateral PF). We
170 wish to make it quite clear that using the wording "preferential flow (PF)" implies structures
171 that permit all types of macropore flow, unstable flow, funnel flow, etc. We recognized that
172 there is no formulation of criteria for determining PF occurrence (Hendrickx and Flury, 2001;
173 Nimmo, 2012). Our method might underestimate the occurrence of PF since it does not
174 necessarily require all the phenomena accounted for by our analysis.

175 **Measurements**

176 To determine soil hydraulic properties (Table 2), representative soil horizons were sampled
177 from each soil pit. Saturated hydraulic conductivities (K_s) were determined with the falling
178 head method using large, 30-cm diameter, undisturbed cores taken near the study hillslope
179 (Lin et al., 2006). Besides, the anisotropic K_s is also accounted for, in which large differences
180 in the lateral and vertical K_s have been found, e.g., the horizontal K_s 10 times higher than the
181 vertical one in the B layer and the vicinity of the bedrock fractures (Table 2). This difference
182 is ascribed to a platy structure due to the geological formation of a long horizontal axis
183 leading to a higher continuity in the horizontal direction along the aggregates/fractures. The
184 water retention characteristics were determined by the pressure plate method, and parameters
185 were fitted using RETC (van Genuchten et al., 1991). The soil texture, bulk density, and total
186 C-content were determined using disturbed soils (Zhao et al., 2010). The precipitation and
187 weather variables required to estimate potential evapotranspiration were recorded by an *in-*
188 *situ* automatic micrometeorological station. Root density, LAI, and coverage of trees were
189 also recorded monthly in this catchment. The groundwater sensor is installed at site 15, and
190 discharge is measured at the lower outlet stream gauge of the catchment (Fig. 1a).

191

192 **Model Evaluation in Simulation of Preferential Flow**

193 In this study, we used the HYDRUS codes (1D, 2D, and 3D) for the water movement
194 simulations (Šimůnek et al., 2006). Practically, we used the HYDRUS-2D as a baseline of the
195 model (i.e., the common model approach) and compared it with the HYDRUS-1D (standard
196 vertical fluxes) and HYDRUS-3D (most complex flux) when the model scale issues were
197 involved (Table 3). Furthermore, based on the calibrated HYDRUS-2D, we assessed the
198 model uncertainties such as expressions of soil and bedrock features and boundary conditions,
199 in predicting the PF.

Governing Flow Equation

200

201 The HYDRUS-2/3D solves the Richards' equation for uniform water flow in

202 saturated/unsaturated domains. The governing flow equation is a modified form of Richard's

203 equation given as:

204 $$\frac{\partial \theta}{\partial t} = \frac{\partial}{\partial x_i}\left(K\left(K_{ij}^A \frac{\partial h}{\partial x_j} + K_{iz}^A\right)\right) - S \qquad\qquad [1]$$

205 where θ is the volumetric water content ($L^3 L^{-3}$), h is the pressure head (L), S is a sink term

206 (T^{-1}), x_i (i = 1, 2, 3) are the spatial coordinates (L), t is time (T), and K_{ij}^A and K_{iz}^A are

207 components of a dimensionless anisotropy tensor K^A, and K is the unsaturated hydraulic

208 conductivity (L T^{-1}), respectively. We used the conventional van Genuchten-Mualem model

209 (van Genuchten, 1980) for the hydraulic functions as follows:

210 $$S_e = \frac{\theta - \theta_r}{\theta_s - \theta_r} = \frac{1}{(1 + |\alpha h|^n)^m} \qquad\qquad [2a]$$

211 $$K = K_s S_e^l [1 - (1 - S_e^{1/m})^m]^2 \qquad\qquad [2b]$$

212 where S_e is the effective saturation, θ_s and θ_r are the saturated and residual water contents (L^3

213 L^{-3}), respectively; the symbols α (L^{-1}), n, and $m = 1-1/n$ are empirical shape parameters; K_s is

214 the saturated hydraulic conductivity (L T^{-1}), and l is a pore connectivity parameter which

215 usually is set to 0.5.

216

217 In comparison with the uniform single-porosity model (Eq. 1), a nonequilibrium dual-

218 porosity model is also used, which assume that water flow is partitioned into a macropore or

219 fracture domain (the inter-aggregate pore domain) and a matrix domain (the intra-aggregate

220 pore domain) where the water does not move at all (Šimůnek et al., 2003). This

221 conceptualization leads to a two-region type flow models that partition the liquid phase into

222 mobile (flowing, inter-aggregate), θ_{mo}, and immobile (stagnant, intra-aggregate), θ_{im}, regions

223 [$L^3 L^{-3}$]: $\theta = \theta_{mo} + \theta_{im}$. The dual-porosity formulation for water flow can be represented as

224 (Gardenas et al., 2006):

225 $$\frac{\partial \theta_{mo}}{\partial t} = \frac{\partial}{\partial x_i}\left(K_{ij} \frac{\partial h}{\partial x_j} + K_{iz}\right) - S_{mo} - \Gamma_w \qquad\qquad [3a]$$

226 $$\frac{\partial \theta_{im}}{\partial t} = -S_{im} + \Gamma_w \qquad\qquad [3b]$$

227 where S_{mo} and S_{im} are sink terms for the mobile and immobile regions, respectively [T^{-1}], and

228 Γ_w is the water transfer rate between the inter- and intra-aggregate pore domains [T^{-1}]. The

229 water mass transfer rate in [3b] is assumed to be proportional to the difference of the pressure

230 head between the macropore and matrix regions (Gerke and van Genuchten, 1993b):

231     $\Gamma_w = \alpha_w(h_f - h_m)$ [3c]

232   where a_w is a first-order mass transfer coefficient ($L^{-1}T^{-1}$):

233     $\alpha_w = \frac{\beta}{d^2} K_a(h)\gamma_w$ [3d]

234   where d is an effective diffusion path-length (i.e., half the aggregate width) (L), β is a shape

235   factor that depends on the geometry of the soil aggregates (-), γ_w is a scaling factor (-), and

236   K_a is the effective hydraulic conductivity of the fracture–matrix interface (L T^{-1}) determined

237   as a simple arithmetic average involving both h_f and h_m as:

238     $K_a(h) = 0.5[K_a(h_f) - K_a(h_m)]$ [3e]

239   **Model Domain, Initial, and Boundary Conditions**

240   We designed the 3D simulated domain of 85 m length, 3 to 8 m width, and 1 to 4 m depth

241   with a slope from 7% to 38% (Fig. 1 and Table 1). Based on soil horizon, the soil profiles

242   were divided into 18 materials characterized by depth-related soil hydraulic parameters, with

243   four layers for the hilltop and four layers mid-slope, five layers down-slope (swale) and five

244   layers outlet parts, respectively. Based on this, the 2D simulation domain was considered as

245   transect without width, and 1D simulation was the vertical soil profile with the heterogeneous

246   soil layers at each of the four locations. The 3D model domain was implemented by

247   importing the Shale Hills hillslope DEM (digital elevation model; x-, y-, z-coordinates of the

248   surface and bedrock topography). The DEM of the catchment was interpolated from light

249   detecting and ranging (LiDAR) elevation point clouds collected by an airplane flown over the

250   catchment in 2006 (PAMAP, PA Department of Conservation and Natural Resources).

251   Approximately 40,000 LiDAR elevation points were interpolated into a 1 m x1 m DEM using

252   ArcGIS 9.2 (ESRI Inc., Redland, CA, USA). Based on this geometric information, we

253   generated a finite element mesh containing 46,200 nodes and resulted in 80,959 3D elements

254   (grid cells) in the form of triangular prisms. The transition into the deeper bedrock was

255   represented by an inclined planar base surface (Fig. 1b). A triangular grid did the

256   discretization of the model area with the intersections of the adjoined triangles referred to as

257   nodes. The grid was spaced <1 cm in the soil domain to ensure numerical stability, with the

258   grid being denser in the topsoil and at the boundaries between layers.

259

260   Model initial conditions were set by linear interpolation of soil moisture at different depths

261   measured at the beginning of the simulation date. The measured daily rainfall and calculated

262   potential evapotranspiration (PET) via the Hargreaves equation were used as a time-variable

263 atmospheric upper boundary condition (BC) of the model domain. Precipitation and PET

264 were additionally corrected for the interception (Šimůnek et al., 2006). The upslope boundary

265 and the two-edges of the domain along the slope were treated as no flux boundaries. A

266 seepage face BC was assigned to the entire width of the lower part of the domain, allowing

267 water to leave the domain under zero potential. A free drainage lower BC was specified for

268 the bottom of the model domain, assuming a unit total vertical hydraulic gradient. The

269 minimum allowed pressure head was considered as 1500 kPa at the upper BC. Root water

270 uptake was based on the model of Feddes et al. (1978). In general, the maximum rooting

271 depth was designed to be 100 cm, with the greatest root density in the upper 50-cm soil depth.

272 **Model Calibration and Implementation**

273 Our multi-dimensional modeling approach essentially corresponds to the three types of PF

274 that occurred in three scales. In the 1D simulation at the pedon scale, depth-related hydraulic

275 parameters represent unstable water flow due to the heterogeneous soil layers (e.g.,

276 macropore flow). In the 2D simulation at the hillslope scale, we further considered the

277 subsurface lateral flow from different sloped positions (e.g., funnel flow due to impeding

278 layer). The 3D simulation at the catchment scale allowed us to consider lateral convergence

279 flow from the surrounding units. To compare different model approaches, the hydraulic

280 properties and boundary conditions for each simulation were parameterized as consistently as

281 possible with independent measurements (Table 3). We first calibrated the HYDRUS-2D

282 model using the two-month data from July and August in 2007 (Fig. 3). For that calibration

283 step, the measured soil hydraulic parameters (i.e., uncalibrated parameters) were used as

284 initial values for the simulations. Table 1 showed that soil horizons varied from loamy sand

285 to sandy loam. The changes in the soil texture also reflect changes in the total porosity and

286 the pore size distribution, as indicated by the depth-related hydraulic parameters (Table 2).

287 For instance, the Weikert soil had a lower saturated water content (θ_s) and a shallow R

288 horizon while Rushtown had a large θ_s and a deep soil depth. We then did the inverse model

289 to optimize the hydraulic parameters. The van Genuchten-Mualem parameters α, n, and K_s

290 were adjusted during the calibration process based on our soil profile moisture measurements

291 at the monitoring sites (Table 2). The calibrated parameters showed much better simulations

292 than the measured one; that is, the peak and range of measured soil water were simulated

293 reasonably (Fig. 3). Therefore, we used the calibrated parameters for all subsequent

294 HYDRUS simulations.

295 **Temporal simulation setting**

296 Although model calibration represented one level of testing to reproduce field data, the model
297 may not be applied to field conditions that are significantly different than the conditions
298 under which calibration was conducted. As also indicated by Melsen et al. (2016), the model
299 calibration and validation time interval should keep pace with the increase in spatial
300 resolution to resolve the processes that are relevant at the applied spatial resolution. For these
301 reasons, it is important to test the predictive capabilities beyond the calibration period. Based
302 on data availability, we designed the simulation time for three temporal scales to cross-
303 examine modeling for various scenarios. The first time scale was minute-based representing
304 the rapid response of water redistribution after rainfall, used to evaluate the occurrence of PF.
305 The second time scale was daily-based, representing the water dynamics associated with
306 cycles of wetting and drying within a hydrological year and was used basically to calibrate
307 and validate the modeling. The third time scale was yearly-based representing the water
308 cycles over multiple years, used to check the power of model predictions for long-term
309 periods.

310 **Model Uncertainties**

311 The simulations of hydrological fluxes are affected by various uncertainties resulting from
312 the soil hydraulic parameterization and boundary conditions (Loos et al., 2007). Firstly, the
313 above-calibrated parameters α, n, and K_s in the single-porosity model were then used as
314 default values for calibration of the dual-porosity model, where only a_w was fitted while
315 others (i.e., θ_s and θ_r) were modified corresponding with the single-porosity model (Table 2).
316 The residual water content is equal to zero for the mobile region (i.e., residual water only
317 present in the immobile region; Clothier et al., 1995). Secondly, to illustrate the consequences
318 of anisotropic hydraulic properties on PF, the model results using anisotropic K_s are
319 compared with the model output from isotropic K_s. For some unmeasured horizontal K_s that
320 are attributed to the fractured bedrock, we used a value that is 10 times the vertical K_s.
321 Thirdly, to examine the effect of fractured shale bedrock, the lower BC was set as either a
322 highly-weathered permeable bedrock (i.e., free drainage) or less-weathered, impermeable part
323 (i.e., no flux) (Tromp-van Meerveld et al., 2007).

324 **Performance Assessment**

325 In addition to graphical displays of simulated and measured results, statistical measures (root
326 mean square error, *RMSE*, and the Nash–Sutcliffe efficiency, *NSE*) were used to evaluate the
327 model performance (e.g., Ebel et al., 2007; Bittelli et al., 2010), as follows:

328 $$RMSE = \sqrt{\frac{1}{N} \sum_{i=1}^{N} (P_i - O_i)^2}$$ [4a]

329 $$NSE = 1 - \frac{\sum_{i=1}^{N}(P_i - O_i)^2}{\sum_{i=1}^{N}(O_i - \bar{O})^2}$$ [4b]

330 where N is the number of observations, P_i and O_i are the simulated and measured values,

331 respectively, and $\bar{O}$ is the mean of the observed values, respectively. The *RMSE* is inversely

332 proportional to model efficiency with smaller *RMSE* values indicating higher model

333 efficiency. The *NSE* efficiency statistic ranges between $-\infty$ and 1, with 1 indicating a perfect

334 match between observed and modeled values and less than zero indicating that the predicated

335 value results in more error than using the average value of the observations.

336

337 **Results**

338

339 **Performance of Multi-dimensional Modeling Approach**

340 Soil moisture was simulated using a multi-dimensional modeling approach for three temporal

341 scales (Figs. 4-6). Regardless of the model approaches, the model performed well in

342 simulating soil moisture trends. We found that the most complex model provided the best

343 predictions of the measured dynamics at each monitoring site. The PF was successfully

344 described by 2D or 3D modeling approaches, but not by 1D simulation (Fig. 4). Notably, 3D

345 modeling simulated the timing of the PF occurrences accurately. While the 3D Richards

346 equation-based numerical model simulated water increases at the R horizon earlier than the

347 above soil layer, the 1D simulation showed the frequent increase from top to down soil at site

348 74. Similarly, at site 51, the 3D simulation showed very well matched to the measured soil

349 moisture at the 40-cm soil depth, which is much earlier and large increases than the above 18-

350 cm soil depth; however, the 1D simulation did not reflect the occurrence of PF. However,

351 even that 3D simulations at site 74 lagged about 6 h behind the measured data at the R

352 horizon, in which water bypassed the upper horizons and reached the subsoil probably related

353 to the water repellency of the organic litter or water recharges originated in the side slope

354 (Lin et al., 2006). Our current model still did not take account of those processes well. The

355 *RMSE* values are all smaller than 0.1, with the 3D simulations having the lowest bias and the

356 1D simulations having the highest bias (Table 4). Similarly, the *NSE* values range from -3.8

357 to 0.74, with the 3D simulation having the most favorable expectations. The results in the

right part of Table 4 seem to agree with the trends previously observed in the figure. We noticed that some *NSE* values are below zero that may illustrate the effect of a few very poorly simulated values in biasing the *NSE*.

For 1-yr hydrological simulations (Fig. 5), the 1D model underestimated the soil moisture because it did not consider the lateral flow contributions. In contrast, the 2D simulation, which considered the sloped-topographic effects, has reflected the occurrence of PF. The 2D simulations did not perform as well as the 3D simulations when comparing daily soil moisture observations and simulations. The 3D simulations provided the best predictions of the measured values, although there are still some differences that are primarily attributed to the spatial variability inherent in hydrological processes (Fig. 5). Figure 6 showed the 2D simulation for the 4-yr period, which showed a very similar predictive power with the 1-yr simulation, indicating the current model can simulate the hydrological processes for the long-term period. Figure 7 shows the simulated water balance in 2007, indicated that 38% of the precipitation was drained (of which 6% was seepage flux and 32% was streamflow), 35% was evaporated, 19% was transpired, and 8% was stored in the soil. The overland flow was a small portion and only occurred after higher rainfall intensity events. Actual evapotranspiration was relatively large for the maple-oak-hickory vegetation compared to the amount of subsurface drainage.

The 3D model enabled predictions to be obtained for soil water content distributions at each location and time, considering convergent lateral inflows. An example of a 3D representation of pressure head on August 21, 2007 (Fig. 8), indicating a higher water potential in the downslope positions or the topsoil depths. Furthermore, we selected a transect of simulation on the same date to show representative subsurface lateral flow after rainfall events (Fig. 9). In this example, PF in the shallow Weikert soil occurred in the R horizon while in the deep soil such as the Rushtown, it happened in the Bw and C horizons. The increases in soil moisture indicate that the water infiltrated into the bedrock fractures below the shallow Weikert soil and moved laterally to the deep horizons of the downslope Rushtown soil. To our best knowledge, this is one of few attempts to capture the PF pathways by using the physically-based model successfully.

Effects of Soil Parameters and Boundary Condition

391   We firstly examined the significance of the nonequilibrium flow in a dual-porosity system.

392   The single-porosity and dual-porosity approaches reflected the soil moisture dynamics

393   throughout a hydrological year (Fig. 10). However, the dual-porosity model provided

394   improved simulations, implying that the model in considering the fracture-matrix structure

395   may have indicated that the area is characterized by a fractured structure, which is the

396   premise of the PF. Besides, the prominence of PF may also be supported by the anisotropic

397   K_s. Expectedly, Figure 11 shows that the simulations improved once the anisotropic K_s was

398   considered, indicating that anisotropy significantly contributed to the rapid subsurface flow.

399   Examination of Table 4 also confirms that the single-porosity model does not perform as well

400   as the dual-porosity model, and considering anisotropic K_s improves the simulations.

401

402   Our results illustrated that the boundary condition is essential for PF simulation. At site 74, a

403   no flux BC provided better predictions than when a permeable BC was assumed (Fig. 12a).

404   However, at site 51, a free drainage BC provides better predictions than when an

405   impermeable BC is taken into account (Fig. 12b). This implied that site 74 was characterized

406   by an impermeable soil-bedrock interface (Table 4), whereas site 51 should be described by

407   permeable shale geology. Furthermore, Figure 14a showed that the model performed well in

408   simulating the water table dynamics at site 15, considering that perched water table and

409   groundwater recharge into the soil may not be fully considered in our model. Furthermore,

410   Figure 14b shows the measured discharge for the whole catchment and simulated discharge

411   in the sub-catchment accounted for (i.e., our 3D domain). Although the values can not be

412   directly compared, the similar trends and dynamics between them should have indicated that

413   our model was sensitive in simulating lateral subsurface drainage from hills to valleys.

414

415   **Discussion**

416

417   **Identification of Preferential Flow using a modeling approach**

418   In our study, direct evidence of PF was obtained by comparing the dynamics in the measured

419   soil moisture contents and further validated by the numerical simulations. The occurrence of

420   PF is illustrated to be governed by internal properties and external influences. Expectedly,

421   one-dimensional hydrological modeling has one general disadvantage in that lateral water

422   fluxes may not be taken into account, in which the external influences are generally identified

423   as input and output fluxes in the vertical dimension. Even the dual-porosity model in 1D

424 simulation, it still failed to capture the macroflow due to it exhibited the sequential flow in
425 the soil profile (Larsson and Jarvis, 1999). During 2D simulation, lateral flow from ridges to
426 valleys was correctly simulated, in which output fluxes from adjacent spatial units are
427 commonly input fluxes to the neighboring spatial units and have been referred to as a
428 catenary linkage along the slopes (Zepp et al., 2005). Our results recognized that the 2D
429 simulations did not perform well as the 3D simulations predicted the PF. During the 3D
430 simulations, the lateral convergence flow from the surrounding units strongly contributed to
431 the PF dynamics, especially in the concave hillslope position (e.g., site 51). Those model
432 findings are consistent with the previously observed analysis that lateral/inter-connected flow
433 frequently occurred in this sloped forest (Grahamm and Lin, 2011). While the 3D physics-
434 based modeling has previously been restricted in a complex landscape (Loague et al., 2006;
435 Mirus et al., 2007), our study addressed the necessity to perform 3D simulations with the
436 reasonable parametrization to describe the PF components and pathways adequately. Tromp-
437 van Meerveld and Weiler (2008) indicated that the inclusion of PF in the model influenced
438 the distribution of the maximum saturation depths at the soil-bedrock interface and increased
439 peak flows and recessions. At their studied Panola hillslope, several process-based modeling
440 studies have taken into account the detailed representation of hydrologic and
441 hydrostratigraphic variables (Hopp and McDonnell, 2009; James et al., 2010; Camporese et
442 al., 2019). However, their model did not strictly capture the PF dynamics, particularly in
443 terms of validating with the field observations.
444

Effects of Soil Parameters in Simulating Preferential Flow

446 Numerous studies have shown that flow processes in soils can be better described using
447 nonequilibrium two-domain models rather than classical single-domain models (e.g.,
448 Šimůnek et al., 2003; Kohne et al., 2004). Our results confirm that, in comparison with a
449 single-domain model, dual-porosity models do perform well in describing the processes
450 within the local soil subsurface macropore network and better represent the dynamics of soil
451 moisture (McDonnell et al., 2007). Studies have also mentioned that soils consisting of fine
452 layers parallel to the surface, like stratified soils, have a horizontal K_s that is greater than the
453 vertical K_s (e.g., Newman et al., 1998; Beckwith et al., 2003). In the same studied area, Guo
454 et al. (2019) showed that water movement is almost parallel to the lateral slope. This
455 observation might explain why the simulations that consider the anisotropy of K_s produce
456 better prediction results than that considered isotropic K_s. In our simulation, the contrast of

457 anisotropy is somewhat like the ratio of soil to bedrock in the fractured zone. It is expected
458 that omitting the anisotropy in hydraulic parameters will negatively affect simulation results
459 (Ebel et al., 2007; James et al., 2010). The inference is that the anisotropic K_s is more realistic
460 in representing the macroporosity found in the structured soil and that the studied watershed
461 was characterized by weathered and un-weathered bedrocks that contribute a lateral flow
462 pathway.

463

Effects of Boundary Conditions in Simulating Preferential Flow

465 We demonstrated that the representation of fractured shale geology is essential to simulate
466 the occurrence of PF accurately. Although the bedrock is typically assumed as an
467 impermeable layer in numerical models, there is evidence indicating that bedrock sometimes
468 is permeable (e.g., Comporese et al., 2019). Our results show that actual field conditions may
469 be more accurately characterized by considering both a permeable fracture-structured shale
470 bedrock (e.g., site 51) and an impermeable bedrock (e.g., site 74). This finding was
471 corroborated by Ebel et al. (2007), who indicated that representing layered geologic
472 interfaces by an impermeable boundary condition leads to significant prediction errors.
473 Several other researchers have also documented the role of soil-bedrock interfaces as
474 important hillslope flow paths (e.g., Freer et al., 1997; Onda et al., 2001). Lin et al. (2006)
475 described a discontinuity in the fragipan and noted that a significant error in perched water
476 depths could be caused by a minimal mistake in simulated soil water contents, and vice versa.
477 In this regard, our inability to continuously parameterize the structure and geometry of sub-
478 catchment may have prevented detailed assessments of the weathered bedrock water table
479 response and discharge (Fig. 13), as well as the soil moisture dynamics. The more
480 sophisticated geological characterization will be needed to improve model predictions
481 (Rakovec et al., 2016).

482

Pathway and Connectivity along the Hillslope

484 It was determined that hyper-resolution monitoring data of soil moisture might be used to
485 address the occurrence of PF at the point scale. Combined with a model survey, potential
486 spatial flow patterns may be identified, flow mechanisms may be confirmed, and flow
487 pathways may be documented at the hillslope scale (Sidle et al., 2001; Salve et al., 2012; Fan
488 et al., 2019). The connectivity of flow paths is highly related not only to the soil-bedrock
489 properties but also to the initial moisture content (Salve et al., 2012). Although PF occurred at

490   each site, only a few rainfall events led to connectivity from the hilltop to the valley floor

491   (data in the supplement file; Lin and Zhou, 2008). Especially during the initial soil dry

492   condition and/or combined the short-lasting and intense rainfall event, while lateral

493   macropore flow was dominant in the planar uphill position, a combination of vertical

494   macropore flow and lateral matrix flow was dominant in the concave midslope position. This

495   suggested that during dry conditions, the flow paths for the occurrence of PF are only 'locally'

496   connected and can be activated to deliver water through long distances to the valley floor

497   (Guo et al., 2014), as illustrated by the simulation in Figure 8. It is also likely that a perched

498   water table developed in the shallow subsurface and resulted in the water flow towards the

499   downslope position, as was indicated by a rapid rise of topsoil water after large precipitation

500   events at site 15 (Fig. 13a). The presence of a perched water table indicated that the vertical

501   percolation locally exceeded the K_s at the perching layers and suggested that flow paths may

502   not be vertical through the entire thickness of the unsaturated zone. Instead, water has

503   diverted laterally to a fault zone or another high-permeability channel that channeled

504   downward to the water table.

505

506   For a conceptual understanding of modeling findings, we present a flow diagram (Fig. 14) by

507   summing up two types of subsurface lateral flow as dominating hydrological features, which

508   were highly controlled by multiscale behavior of the intrinsic soil and fracture system. The

509   first pathway that PF was initiated when the rainfall infiltrated the shallow impermeable

510   bedrock at the upslope, where water moves laterally, recharged the Bw and C horizons of the

511   mid-slope and downslope, and finally recharged the Bt horizon and the C horizon of the

512   valley floor. A second pathway had water moving through the fracture and directly recharged

513   the deep C horizon at the downslope and valley floor sites. This constituted a hydrological

514   pathway for rapid lateral flow above the groundwater zone, especially during the initial soil

515   wet condition, and/or associated with the long-lasting and intermittent rainfall.

516

Implications and Beyond of model simulation

518   In this study, we compared different conceptual approaches to simulate the PF paths in soils.

519   Based on the monitoring evidence of PF and identification of geomorphological conditions,

520   we explored an efficient model approach to confirm our former assumption that subsurface

521   lateral flow is the primary flow mechanism in this catchment (Lin et al., 2006). The

522   HYDRUS model results provide an excellent approximation that describes potential

523 hydrologic flow paths for a complex hillslope structure underlain by fractured bedrocks. The
524 simulations reported herein demonstrate that Richards equation-based numerical models, like
525 HYDRUS, can characterize detailed spatio-temporal hydrologic responses, developing the
526 concepts of the process-based multiscale model, and representing PF paths. The field-based
527 observations and hydrologic-response simulations from the Shale Hills catchment highlight
528 the evidence in simulating fractured bedrock water flow within a complex small catchment
529 and have important implications for understanding hydrologic response in these types of
530 catchment basins.

531

532 In comparison with the previous researches, our modeling application led to several
533 improvements: 1) the full 3D simulation parameterized by the detailed field observations,
534 followed by validation via the experimental data, which provides greater feedback for the
535 understanding of process-based concepts (Fan et al., 2019). In the past, it lacks in the
536 evaluation of scales since we do not adequately perform on small-scale processes integrating
537 up to larger scales (Beven et al., 2020), and thus a Richards equation-based model like
538 HYDRUS may only be applied in the small scale or the relatively simple geomorphological
539 conditions; 2) the characterization of soil hydraulic properties that includes PF via
540 macropores and fractures, and a more accurate description of the subsurface as a multi-layer
541 soil profile above the bedrock (Rakovec et al., 2016). Comparison of hydrologic-response
542 simulations using lab measured soil-water retention curves versus inversely estimated
543 parameters combined with the field moisture measurement showed that integrating soil data
544 with detailed hydrological information (e.g., interflow) can dramatically improve the
545 simulation; 3) the explicit consideration of the anisotropic hydraulic parameters that is
546 virtually ignored in the hydrological calculations (McDonnell et al., 2007). This is a
547 challengeable area given the near impossibility of making the field measurements to assess
548 how soil anisotropy and bedrock permeability influence PF (James et al., 2010; Camporese et
549 al., 2019); and 4) the variable representation of boundary conditions considering that our area,
550 as well as many forest hillslopes composed of relatively thin, permeable soil mantles
551 overlaying less-permeable bedrock (Camporese et al., 2019). In the previous study, lacking
552 presentation of layered geologic interfaces with an assumption of impermeable BC leads to
553 substantial inaccuracies.

554

555 Earth System Models are essential tools for understanding the dominant hydrological
556 processes. Still, they cannot explicitly resolve the first-order structures and functions that

557 fundamentally organize water and energy across the landscapes (Fan et al., 2019). Recently,
558 Camporese et al. (2019) confirmed that Richards equation-based numerical model (CATHY)
559 could generate threshold-driven hillslope responses, e.g., fill and spill mechanism at Panola
560 Mountain Research Watershed. It is promising to further investigate either whether the
561 HYDRUS can reproduce threshold mechanisms or to what extent the fill and spill process
562 exists in a well-gauged Shale Hills catchment. At the same catchment, based on the ground-
563 penetrating radar survey, Guo et al. (2014) found that soil moisture at specific hillslope
564 locations may work as necessary "nodes" and the soil horizon may function as a "path" in the
565 subsurface flow network. They established a conceptual fill-and-spill model of subsurface
566 runoff generation to describe the roles of PF in subsurface hydrology (Guo et al., 2019).
567 Process understanding, data collection, and model development should be linked so that a
568 complete representation can be obtained with each iteration (Grayson and Blöschl, 2000).
569 Still, it is challenging to describe the finer-scaled (meters) principle hillslope structure
570 representing by a physically-based model into the larger-scaled (kilometers) earth system
571 model, which again recalled the scaling issue (Clark et al., 2017). Currently, the limited
572 availability of the less-than-perfect observed data sets had restricted the field validation of PF
573 models. Without detailed field measurements, it is unlikely that our modeling approach
574 would have identified fractured bedrock flow as an essential process (Beven et al., 2020).
575 Provided such data are available, our results indicate that physically-based models, like
576 HYDRUS, when accurately parameterized, can simulate catchment-scale water flow (Fan et
577 al., 2019).

578

Conclusions

580 In this showcase application, we compared increasingly complex models with a consistent
581 dataset. We concluded that a multi-dimensional modeling approach helped to elucidate how
582 PF processes are affected by soil-landscape features in a small catchment. The model results
583 verified that detailed characterization of soil and bedrock thickness is critical for simulating
584 pore-water pressure generation at sites like Shale Hills, where the convergent subsurface flow
585 is essential. We found that: 1) when the PF was considered in 2D and 3D simulations, it
586 improved the model predictions; 2) the dual-porosity model outperformed the single-porosity
587 model since it can well delineate macropores in the soil, with consideration of anisotropic K_s
588 further improving the model accuracy; and 3) models considering the presence of fractured
589 bedrock performed better than when this was not considered and demonstrated that the actual

field conditions were characterized by fractured bedrock. Further study is expected to examine the robustness of the multi-dimensional process-based hydrological modeling under varying conditions.

Acknowledgments

References

Beckwith, C.W., A.J. Baird, and A.L. Heathwaite. 2003. Anisotropy and depth-related heterogeneity of hydraulic conductivity in a bog peat. II: Modelling the effects on groundwater flow. *Hydrological Processes*, 17, 103–113.

Beven, K., 2001. On explanatory depth and predictive power. *Hydrological Processes*, 15, 3069–3072.

Beven K., and P. Germann. 2013. Macropores and water flow in soils revisited. *Water Resources Research*, 49, doi:10.1002/wrcr.20156.

Beven K., and P. Germann. 1982. Macropores and water flow in soils. *Water Resources Research*, 18, 1311-1325.

Beven, K., Asadullah, A., Bates, P., Blyth, E., Chappell, N., Child, S., …and T., Wagener. 2020. Developing observational methods to drive future hydrological science: Can we make a start as a community? *Hydrological Processes*, 34, 868–873, https://doi.org/10.1002/hyp.13622.

Blöschl, G., and R.B. Grayson. 2001. Spatial Patterns in Catchment Hydrology: Observations and Modelling, 416 pp., Cambridge Univ. Press, New York.

622 Binley, A., Hubbard, S.S., Huisman, J.A., Revil, A., Robinson, D.A., Singha, K., and Slater,
623   L.D. 2015. The emergence of hydrogeophysics for improved understanding of
624   subsurface processes over multiple scales. *Water Resources Research*, 51, 3837–3866.
625   https//doi.org/10.1002/2015WR017016.

626 Bittelli, M., F. Tomei, A. Pistorcchi, M. Flury, J. Boll, E.S. Brooks, and G. Antolini. 2010.
627   Development and testing of a physically based, three-dimensional model of surface and
628   subsurface hydrology. *Advance in Water Resources*, 33, 106–122.

629 Buttle, J.M., and D.J. McDonald. 2002. Coupled vertical and lateral preferential flow on a
630   forested slope. *Water Resources Research*, 38:1060, doi:10.1029/2001WR000773.

631 Camporese, M., Paniconi, C., Putti, M., and McDonnell, J.J. 2019. Fill and spill hillslope
632   runoff representation with a Richards equation-based model. *Water Resources Research*,
633   55. https://doi.org/10.1029/2019WR025726.

634 Clark, M.P., Fan, Y., Lawrence, D.M., Adam, J.C., Bolster, D., Gochis, D.J., et al. 2015.
635   Improving the representation of hydrologic processes in Earth System Models. *Water*
636   *Resources Research*, 51, 5929–5956. https://doi.org/10.1002/2015WR017096.

637 Clark, M.P., Bierkens, M.F.P., Samaniego, L., Woods, R.A., Uijlenhoet, R., Bennett, K.E.,
638   Pauwels, V.R.N., Cai, X., Wood, A.W., and C.D. Peters-Lidard. 2017. The evolution of
639   process-based hydrologic models: historical challenges and the collective quest for
640   physical realism. *Hydrology and Earth System Sciences*, 21, 3427–3440.

641 Durner, W. 1994. Hydraulic conductivity estimation for soils with heterogeneous pore
642   structure. *Water Resources Research*, 30, 211–233.

643 Ebel, B.A., K. Loague, J.E. Vanderkwaak, W.E. Dietrich, D.R. Montgomery, R. Torres, and
644   S.P. Anderson. 2007. Near-surface hydrologic response for a steep, unchanneled
645   catchment near Coos Bay, Oregon: 2. Physics-based simulations. *America Journal of*
646   *Science*, 307, 709–748.

647 Fan, Y., Clark, M., Lawrence, D.M., Swenson, S., Band, L.E., Brantley, S. L., et al. 2019.
648   Hillslope hydrology in global change research and Earth System Modeling. *Water*
649   *Resources Research*, 55, 1737–1772. https//doi.org/10.1029/2018WR023903.

650 Feddes, R.A., P. Kabat, P.J.T. van Bakel, J.J.B. Bronswijk, and J. Halbertsma. 1988.
651   Modelling soil water dynamics in the unsaturated zone-State of the art. *Journal of*
652   *Hydrology*, 100, 69–111.

653 Feddes, R.A., P.J. Kowalik, and H. Zaradny. 1978. Simulation of field water use and crop
654   yield, John Wiley and Sons, New York, NY.

655 Freer, J., McDonnell, J.J., Beven, K.J., Brammer, D., Burns, D., Hooper, R. P., and Kendall,
656   C. 1997. Topographic controls on subsurface storm flow at the hillslope scale for two
657   hydrologically distinct small catchments. *Hydrological Processes*, 11, 1347–1352.

658 Freeze, R.A. 1972. Role of subsurface flow in generating surface runoff 1. Base flow
659   contributions to channel flow. *Water Resources Research*, 8, 609–624.

660 Gardenas, A.I., J. Šimůnek, N. Jarvis, and M.Th. Van Genuchten. 2006. Two-dimensional
661   modelling of preferential water flow and pesticide transport from a tile-drain field.
662   *Journal of Hydrology*, 329, 647–660.

663 Gao, M., Li, H.-Y., Liu, D., Tang, J., Chen, X., Chen, X., Blöschl, G., and L.R. Leung. 2018.
664   Identifying the dominant controls on macropore flow velocity in soils: A meta-analysis.
665   *Journal of Hydrology*, 567, 590–604.

666 Gerke, H.H., and M.T. van Genuchten. 1993a. A dual-porosity model for simulating the
667   preferential movement of water and solutes in structured porous media. *Water Resources*
668   *Research*, 29, 305–319.

669 Gerke, H.H., and M.T. van Genuchten. 1993b. Evaluation of a first order water transfer term
670   for variably saturated dual-porosity flow models. *Water Resources Research*, 29, 1225–
671   1238.

672 Graham, C., and H.S. Lin. 2011. Controls and frequency of preferential flow occurrence at
673   the Shale Hills Critical Zone Observatory: A 175 event analysis of soil moisture
674   response to precipitation. *Vadose Zone Journal,* 10, 816–831.

675 Grayson, R., Blöschl, G., 2000. Spatial modelling of catchment dynamics. In: Grayson, R.,
676   Blöschl, G. (Eds.), Spatial Patterns in Catchment Hydrology: Observations and
677   Modelling. Cambridge University Press.

678 Gu, W.Z., J.F. Liu, H.S. Lin, J. Lin, H.W. Liu, A.-M. Liao, N. Wang, W.Z. Wang, T. Ma, N.
679   Yang, X.G. Li, P. Zhuo, and Z. Cai. 2018. Why hydrological maze: The
680   hydropedological trigger? Review of experiments at Chuzhou Hydrology Laboratory.
681   *Vadose Zone Journal*, 17, 170174. doi:10.2136/vzj2017.09.0174.

682 Guo, L., H.S. Lin, and J. Chen. 2014. Subsurface lateral flow network on a hillslope revealed
683   by time-lapse ground penetrating radar. *Water Resources Research*, 50, 9127–9147.

684 Guo, L., H. Lin, B. Fan, J. Nyquist, L. Toran, G. Mount. 2019. Preferential flow through
685   shallow fractured bedrock and a 3D fill-and-spill model of hillslope subsurface
686   hydrology. *Journal of Hydrology*, 576, 430–442.

687 Haga, H., Y. Matsumoto, J. Matsutani, M. Fujita, K. Nishida, and Y. Sakamoto. 2005. Flow
688   paths, rainfall properties, and antecedent soil moisture controlling lags to peak discharge

689   in a granitic unchanneled catchment. *Water Resources Research*, 41, W12410,

690   doi:10.1029/2005WR004236.

691 Hendrickx, J.M.H., and M. Flury. 2001. Uniform and preferential flow, mechanisms in the

692   vadose zone, Conceptual Models of Flow and Transport in the Fractured Vadose Zone,

693   National Research Council, National Academy Press, Washington, DC, pp. 149–187.

694 Hopp, L., and J.J. McDonnell. 2009. Connectivity at the hillslope scale: Identifying

695   interactions between storm size bedrock permeability, slope angle and soil depth.

696   *Journal of Hydrology*, 376, 378–391.

697 Kohne, J.M., B. Mohanty, J. Šimůnek, and H.H. Gerke. 2004. Numerical evaluation of a

698   second-order water transfer term for variably saturated dual-permeability models. *Water

699   Resources Research*, 40:W07409, doi:10.1029/2004WR003285.

700 Korres, W., T.G. Reichenau, P. Fiener, C.N. Koyama, H.R. Bogena, T. Cornelissen, R. Baatz,

701   M. Herbst, B. Diekkrüger, H. Vereecken, and K. Schneider. 2015. Spatio-temporal soil

702   moisture patterns-A meta-analysis using plot to catchment scale. *Journal of Hydrology*,

703   520, 326–341.

704 Larsson, M.H., and N.J. Jarvis, 1999. Evaluation of a dual-porosity model to predict field-

705   scale solute transport in a macroporous soil. *Journal of Hydrology*, 215, 153–171.

706 Lin, H. 2006. Temporal Stability of Soil Moisture Spatial Pattern and Preferential flow

707   Pathways in the Shale Hills Catchment. *Vadose Zone Journal*, 5, 317–340.

708 Lin, H. and X. Zhou. 2008. Evidence of preferential flow using soil hydrologic monitoring in

709   the Shale Hills catchment. *European Journal of Soil Science*, 59, 34–49.

710 Liu, H. and H.S. Lin. 2015. Frequency and control of preferential flow: from pedon to

711   catchment scales. *Soil Science Society of America Journal*, 79, 362–377.

712 Loague, K., C.S. Heppner, B.B. Mirus, B.A. Ebel, Q. Ran, A.E. Carr, S.H. BeVille, and J.E.

713   VanderKwaak. 2006. Physics-based hydrologic-response simulation: Foundation for

714   hydroecology and hydrogeomorphology. *Hydrological Processes*, 20(5), 1231–1237.

715 Loos, C., S. Gayler, and S. Priesack. 2007. Assessment of water balance simulations for large

716   scale weighing lysimeters. *Journal of Hydrology*, 335, 259–270.

717 Maxwell, R.M. 2020. Water colour and climate. *Nature Climate Change*, 102–103.

718 Maxwell, R.M., and S.J., Kollet. 2008. Interdependence of groundwater dynamics and land-

719   energy feedbacks under climate change. *Nature Geoscience*, 1, 665–669.

720 Melsen, L.A., Teuling, A.J., Torfs, P.J.J.F., Uijlenhoet, R., Mizukami, N., and Clark, M.P.

721   2016. HESS Opinions: The need for process-based evaluation of large-domain hyper-

722   resolution models. *Hydrology and Earth System Sciences*, 20, 1069–1079.

723 McCord, J.T., D.B. Stephens, and J.L. Wilson. 1991. Hysteresis and state-dependent
724   anisotropy in modeling unsaturated hill slope hydrologic processes. *Water Resources*
725   *Research*, 27, 1501–1518.

726 McDonnell, J.J., Sivapalan, M., Vaché, K., Dunn, S.M., Grant, G., Haggerty, R., Hinz, C.,
727   Hooper, R., Kirchner, J., Roderick, M.L., Selker, J., Weiler, M. 2007. Moving beyond
728   heterogeneity and process complexity: a new vision for watershed hydrology. *Water*
729   *Resources Research*, 43, W07301, DOI:10.1029/2006WR005467.

730 Mirus, B.B., B.A. Ebel, K. Loague, and B.C. Wemple. 2007. Simulated effect of a forest road
731   on near-surface hydrologic response: Redux. *Earth Surface Processes and Landforms*,
732   32(1), 126–142.

733 Mirus, B.B., K. Loague, J.E. VanderKwaak, S.K. Kampf, S.J. Burges. 2009. A hypothetical
734   reality of Tarrawarra-like hydrologic response. *Hydrological Processes*, 23(7), 1093–
735   1103.

736 Newman, B.D., A.R. Campbell, and B.P. Wilcox. 1998. Lateral subsurface flow pathways in
737   a semiarid ponderosa pine hillslope. *Water Resources Research*, 34, 3485–3496.

738 Nimmo, J.R. 2012. Preferential flow occurs in unsaturated conditions. *Hydrological*
739   *Processes*, 26, 786–789.

740 Onda, Y., Y. Komatsu, M. Tsujimura, and J. Fujihara. 2001. The role of subsurface runoff
741   through bedrock on storm flow generation. *Hydrological Processes*, 15, 1693–1706.

742 Rakovec, O., R. Kumar, S. Attinger, and L. Samaniego. 2016. Improving the realism of
743   hydrologic model functioning through multivariate parameter estimation. *Water*
744   *Resources Research*, 52, 7779–7792.

745 Saito, H., J. Šimůnek, and B.P. Mohanty. 2006. Numerical analysis of coupled water, vapor,
746   and heat transport in the vadose zone. *Vadose Zone Journal*, 5, 784–800.

747 Schulz, K., R. Seppelt, E. Zehe, H.J. Vogel, and S. Attinger. 2006. Importance of spatial
748   structures in advancing hydrological sciences, *Water Resources Research*, 42, W03S03,
749   doi:10.1029/2005WR004301.

750 Scanlon, B.R., M. Christman, R. Reedy, I. Porro, J. Šimůnek, and G. Flerchinger. 2002.
751   Intercode comparisons for simulating water balance of surficial sediments in semiarid
752   regions. *Water Resources Research*, doi:10.1029/2001WR001233.

753 Salve, R., D.M. Rempe, and W.E. Dietrich. 2012. Rain, rock moisture dynamics, and the
754   rapid response of perched groundwater in weathered, fractured argillite underlying a
755   steep hillslope. *Water Resources Research*, 48, 1–25.

756 Sidle, R., S. Noguchi, Y. Tsuboyama, and K. Laursen. 2001. A conceptual model of
757   preferential flow systems in forested hillslopes: evidence of self-organization.
758   *Hydrological Processes*, 15, 1675–1692.

759 Šimůnek, J., N.J. Jarvis, M.T. van Genuchten, and A. Gardenas. 2003. Review and
760   comparison of models for describing nonequilibrium and preferential flow and transport
761   in the vadose zone. *Journal of Hydrology*, 272, 14–35.

762 Šimůnek, J., M.T. van Genuchten, and M. Sejna. 2006. The HYDRUS Software Package for
763   Simulating Two- and Three-dimensional Movement of Water, Heat, and Multiple
764   Solutes in Variably-Saturated Media: Technical Manual. Version 1.0. PC-Progress,
765   Prague, Czech Republic.

766 Šimůnek, J., M.Th. van Genuchten, M. Sejna. 2016. Recent developments and applications of
767   the HYDRUS computer software packages. *Vadose Zone Journal*. 15,
768   http://dx.doi.org/10.2136/vzj2016.04.0033.

769 Sivakumar, B. 2004. Dominant processes concept in hydrology: moving forward.
770   *Hydrological Processes*,18, 2349–2353.

771 Todd, M.S., P.R. Jeff, and M.H. George. 2000. Shallow subsurface storm flow in a forested
772   headwater catchment: Observations and modeling using a modified Topmodel. *Water
773   Resources Research*, 36(9), 2575–2586.

774 Tromp-van Meerveld, I., and M. Weiler. 2008. Hillslope dynamics modeled with increasing
775   complexity. *Journal of Hydrology*, 361, 24–40. DOI: 10.1029/2007WR006299.

776 Tromp-van Meerveld, H.J. and J.J. McDonnell. 2006. Threshold relations in subsurface
777   stormflow 1. A 147 storm analysis of the Panola hillslope. *Water Resources Research*,
778   42, W02410, doi:10.1029/2004WR003778.

779 Tromp-van Meerveld, H.J., N.E. Peters, J.J. McDonnell. 2007. Effect of bedrock permeability
780   on subsurface stormflow and the water balance of a trenched hillslope at the Panola
781   Mountain Research Watershed, Georgia, USA. *Hydrological Processes*, 21, 750–769.

782 Twarakavi, N.K.C., Šimůnek, J., Seo, H.S. 2008. Evaluating interactions between
783   groundwater and vadose zone using HYDRUS-based flow package for MODFLOW.
784   *Vadose Zone Journal*, 7, 757–768.

785 van Genuchten, M.T. 1980. A closed-form equation for predicting the hydraulic conductivity
786   of unsaturated soils. *Soil Science Society of America Journal*, 44, 892–898.

787 van Genuchten, M.T., F.J. Leij, and S.R. Yates. 1991. The RETC code for quantifying the
788   hydraulic functions of unsaturated Soils. Ver. 1.0 EPA Rep. 600/2-91/065. U.S. Salinity
789   Lab., USDA-ARS, Riverside, CA.

790 Vereecken, H., J.A. Huisman, H.J. Hendricks Franssen, N. Brggemann, H.R. Bogena, S.
791   Kollet, M. Javaux, J. van der Kruk, and J. Vanderborght. 2015. Soil hydrology: Recent
792   methodological advances, challenges, and perspectives. *Water Resources Research*, 51,
793   2616–2633.

794 Vogel, H.-J., and K. Roth. 2003. Moving through scales of flow and transport in soil. *Journal*
795   *of Hydrology*, 272, 95–106.

796 Weiler, M., and J.J. McDonnell. 2004. Virtual experiments: a new approach for improving
797   process conceptualization in hillslope hydrology. *Journal of Hydrology*, 285, 3–18.

798 Whipkey, R.Z. 1965. Subsurface stormflow from forested slopes. *Bulletin-International*
799   *Association of Scientific Hydrology*, 10, 74–85.

800 Zepp, H., J.L. Tang, and B. Zhang. 2005. A methodological framework for a multiscale study
801   on hydrological processes and soil erosion in subtropical SE China. *Pedosphere*. 15,
802   695–706.

803 Zhao, Y., S. Peth, R. Horn, J. Krümmelbein, B. Ketzer, Y.Z. Gao, J. Doerner, C. Bernhofer,
804   and X.H. Peng. 2010. Modelling grazing effects on coupled water and heat fluxes in
805   Inner Mongolia grassland. *Soil and Tillage Research*, 109, 75–86.

806 Zhao, Y., J. Tang, C. Graham, Q. Zhu, K. Takagi, and H. Lin. 2012. Hydropedology in the
807   ridge and valley: soil moisture patterns and preferential flow dynamics in two
808   contrasting landscapes. In: Lin, Henry (Ed.), Hydropedology: Synergistic Integration of
809   Soil Science and Hydrology. Academic Press.

All Figures and Tables.

Table 1 Soil and landscape features displayed for the monitoring sites 74, 54, 51, and 15 in the Shale Hills catchment of Pennsylvania.

Soil series	Site number	Landform position	Slope/%	Soil horizon	Sensor depth/cm	Depth to bedrock/cm	Rock fragment/%	Soil texture
Weikert	74	Nearly planar upslope	23.8	Oe-A	5	22		
				A	8		0	Silt loam
				A-CR	10		60	Silt loam
				CR	17		90	Silt loam
				R	37			
Rushtown	53	Swale, upslope	38.4	A	10	>150	5	Silt loam
				Bw1	22		5	Silt loam
				Bw2	44		5	Silt loam
				Bw3	73		5	Silty clay loam
				C	123		80	
Rushtown	51	Swale, midslope	13.1	Oe-A	5	>300		
				A	8		5	Silt loam
				A-Bw1	12		5	Silt loam
				Bw1	15		5	Silt loam
				Bw2	22		5	Silt loam
				Bw3	40		5	Silty clay loam
				BC	68		50	Silty clay loam
				BC-C1	92		50	Silty clay loam
				C1	122		80	
				C2	162		80	
Ernest	15	Valley floor	6.6	A	13	> 300	0	Silt loam
				AE-Bw	20		0	Silt loam
				Bt	41		0	Silty clay
				Bt-C2	52		0	Silty clay
				C2	72		80(soft)	Sandy loam
				C2-C3	85		0	Clay
				C4	109		90 (soft)	Sandy loam

Table 2 Hydraulic parameters for the different monitoring sites: (a) single-porosity model with van Genuchten-Mualem parameters obtained from inverse modeling with field data, (b) dual-porosity model parameters obtained from inverse modeling with field data (immobile water parameters indicated by subscript im, and mobile water parameters indicated by subscript mo). a_w is a first-order mass transfer coefficient.

Site	Soil depth (cm)	(a) single-porosity model						(b) dual-porosity model				
		θ_r (cm^{3}cm^{-3})	θ_s (cm^{3}cm^{-3})	α (cm^{-1})	n (-)	$K_s(K_v/K_h)$ (cm d^{-1})	l (-)	θr_{mo} (cm^{3}cm^{-3})	θs_{mo} (cm^{3}cm^{-3})	θr_{im} (cm^{3}cm^{-3})	θs_{im} (cm^{3}cm^{-3})	a_w (cm^{-1}d^{-1})
74	0-5	0.020	0.260	0.247	1.523	316/80	0.5	0	0.160	0.020	0.100	1.839E-04
	5-15	0.000	0.290	0.036	1.714	3003/265	0.5	0	0.190	0.000	0.100	1.098E-03
	15-30	0.030	0.250	0.020	1.547	301/320	0.5	0	0.100	0.030	0.150	7.198E-01
	30-76	0.040	0.400	0.022	1.473	109/560	0.5	0	0.150	0.040	0.250	1.934E-04
53	0-10	0.000	0.440	0.007	2.277	1123/159	0.5	0	0.350	0.000	0.090	5.953E-04
	10-40	0.040	0.380	0.008	2.089	5/245	0.5	0	0.300	0.040	0.080	2.066E-05
	40-80	0.040	0.330	0.021	1.594	293/370	0.5	0	0.180	0.040	0.150	5.579E-03
	80-149	0.010	0.260	0.006	1.846	318/690	0.5	0	0.150	0.010	0.110	5.930E-04
51	0-10	0.030	0.400	0.080	1.580	150/116	0.5	0	0.360	0.030	0.040	2.000E-04
	10-30	0.050	0.450	0.011	3.461	602/270	0.5	0	0.350	0.000	0.150	9.301E-03
	30-50	0.030	0.330	0.012	2.278	144/2100	0.5	0	0.200	0.000	0.160	2.623E-03
	50-100	0.050	0.300	0.037	1.801	299/410	0.5	0	0.150	0.080	0.120	2.056E-03
	100-236	0.030	0.300	0.009	2.095	2/450	0.5	0	0.160	0.050	0.140	6.651E-03
	0-20											
15	20-52	0.050	0.450	0.023	2.228	27/170	0.5	0	0.390	0.050	0.060	5.390E-04
	52-83	0.080	0.430	0.013	1.962	2485/230	0.5	0	0.330	0.080	0.100	1.134E-05
	83-91	0.120	0.420	0.012	1.716	273/320	0.5	0	0.290	0.100	0.150	2.024E-04
	91-260	0.100	0.370	0.100	1.450	100/310	0.5	0	0.250	0.100	0.120	2.000E-04
	0-10	0.130	0.350	0.014	1.355	57/130	0.5	0	0.200	0.100	0.180	2.038E-04

Table 3 Design of the multi-dimensional, i.e., 1D, 2D, and 3D modeling approaches and its corresponding uncertainty comparisons used in the study. single-porosity model (VG), dual-porosity model (DP), fractured bedrock (FB), impermeable bedrock (IB), isotropy K_s (Iso) and anisotropy K_s (Ani). Y: available; N: not available.

Scale	soil hydraulic parameterization			K_s		boundary	
	VG	DG		Iso	Ani	IB	FB
2D (baseline)	Y	Y		Y	Y	Y	Y
1D	Y	N		Y	N	Y	N
3D	Y	N		Y	N	Y	N

Table 4 Nash–Sutcliffe efficiency (*NSE*) values and root mean square errors (*RMSE*) of the 1D, 2D, and 3D modeling approaches during the hydrological year 2007 at the sites 74 and 15 as used in the single-porosity model (VG), impermeable bedrock (IB), and Isotropy K_s. The model uncertainty comparisons included the corresponding 2D simulations of the dual-porosity model (DP), fractured bedrock (FB), and anisotropy K_s (Ani).

Site	soil	simulation using the single-porosity model (VG), impermeable bedrock (IB) and Isotropy K_s						model uncertainty comparisons					
	depth	*NSE*			*RMSE*			*NSE*			*RMSE*		
	(cm)	1D	2D	3D	1D	2D	3D	DP	FB	Ani	DP	FB	Ani
74	5	-0.319	0.122	**0.705**	0.045	0.021	0.021	-0.153	-0.282	0.220	0.020	0.050	0.023
	10	0.169	0.399	**0.737**	0.035	0.024	0.020	0.296	0.329	0.360	0.018	0.031	0.018
	17	-2.047	**0.534**	**0.646**	0.068	0.020	0.023	**0.623**	0.456	-2.223	0.017	0.029	0.18
	37	-2.538	-0.195	-0.087	0.036	0.021	0.020	0.475	-1.330	-16.823	0.017	0.029	0.019
51	18	-1.562	-1.026	0.312	0.067	0.059	0.034	0.239	0.498	-0.256	0.036	0.030	0.049
	40	-0.627	-0.307	0.439	0.042	0.050	0.025	0.191	**0.516**	-0.127	0.029	0.023	0.040
	92	-0.441	0.017	0.222	0.032	0.026	0.023	0.128	**0.567**	0.036	0.024	0.015	0.021
	162	-3.790	-2.558	-3.448	0.044	0.074	0.043	-2.015	-0.676	-2.874	0.035	0.026	0.040
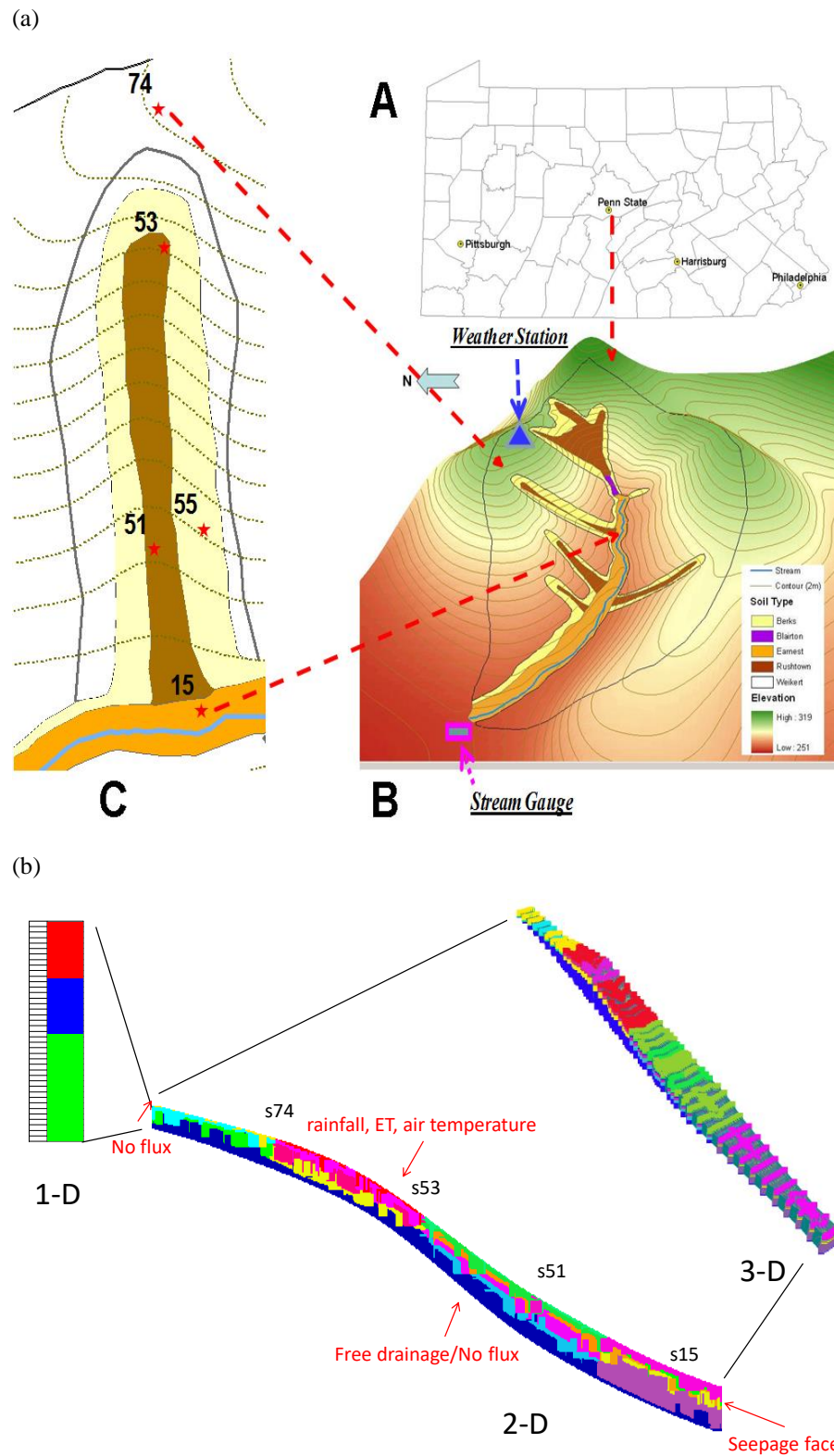
Figure 1. (a) Location (A) and shape (B) of the Shale Hills catchment, and the study hillslope (C), and (b) graphical representation of the HYDROUS-1D, -2D, and -3D simulation approaches used for the soil domain with 18 different soil materials as characterized by the different colors for the monitoring sites 74 (s74), 53 (s53), 51 (s51), and 15 (s15) with the applied boundary conditions.

(a)
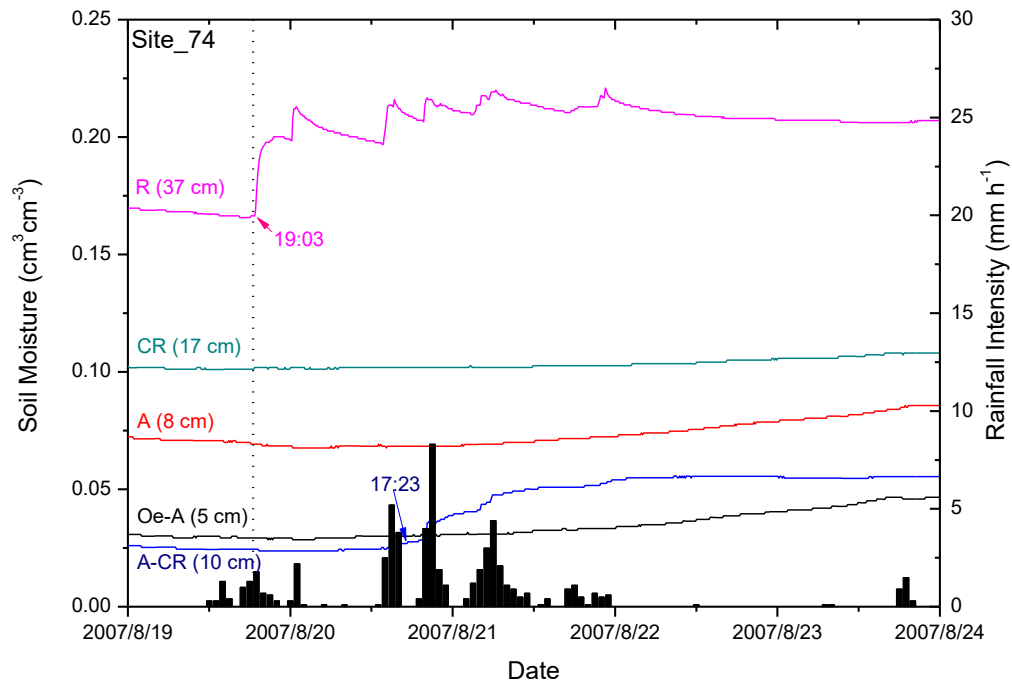
(b)
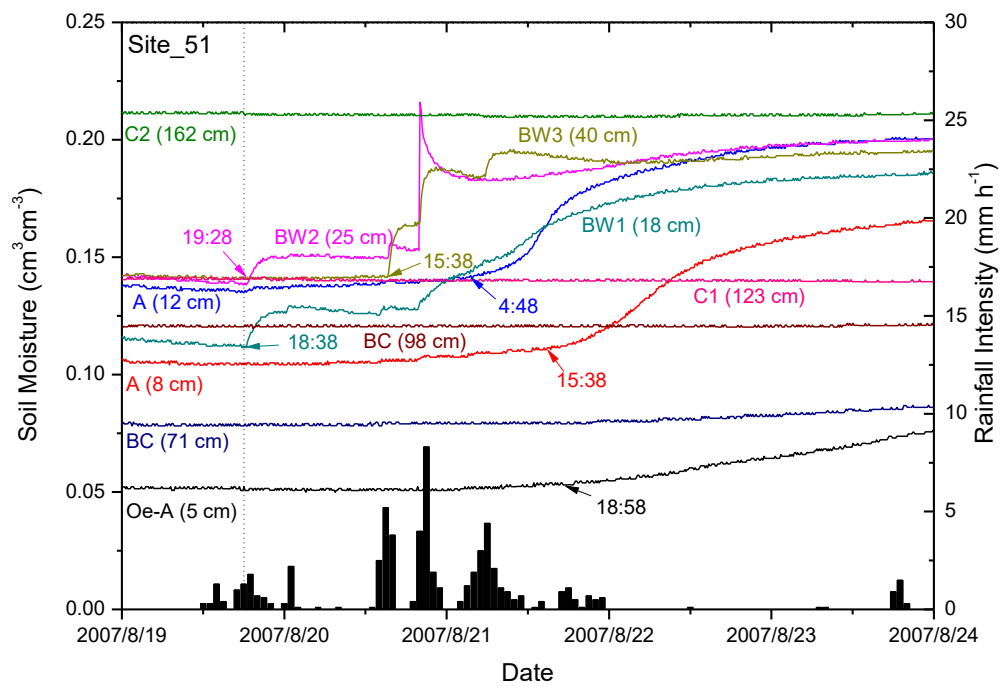
Figure 2. Minute-based volumetric soil moisture contents and rainfall intensities displayed over time during the drier period of August 19-24, 2007 at site_74 (a) and site_51 (b). The time at which soil moisture contents started to increase following a rainfall event is indicated by bold arrows. The different colored lines identify the soil horizons with the horizon layer in capital letters and the depth of soil moisture content in parenthesis.

(a)
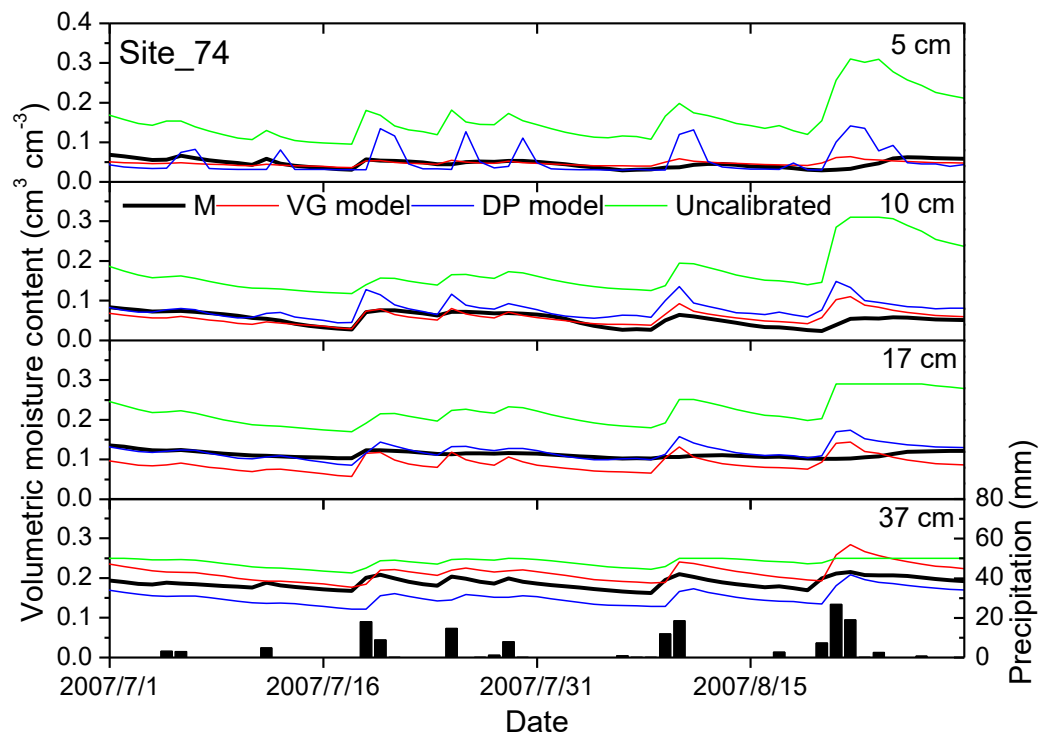
(b)
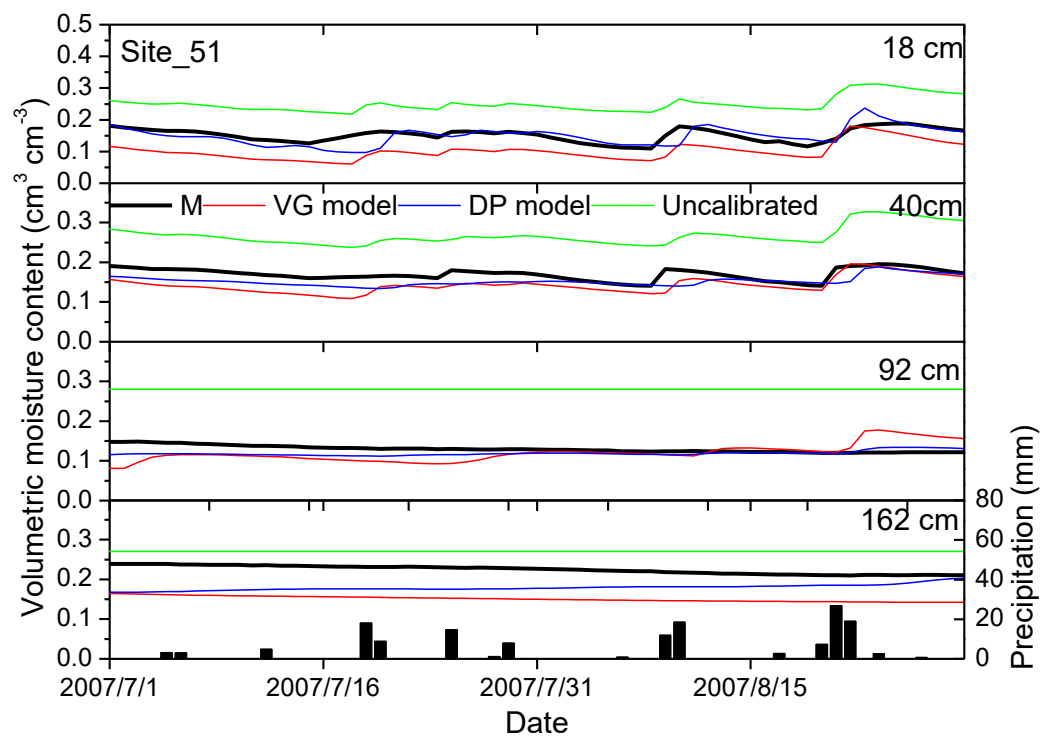
Figure 3. Comparison of the predicted and measured soil moisture values and rainfall quantities displayed over time for use in the HYDRUS-2D model calibrations at site 74 (a) and site 51 (b). uncalibrated: initial laboratory-measured hydraulic parameters.

(a)

(b)
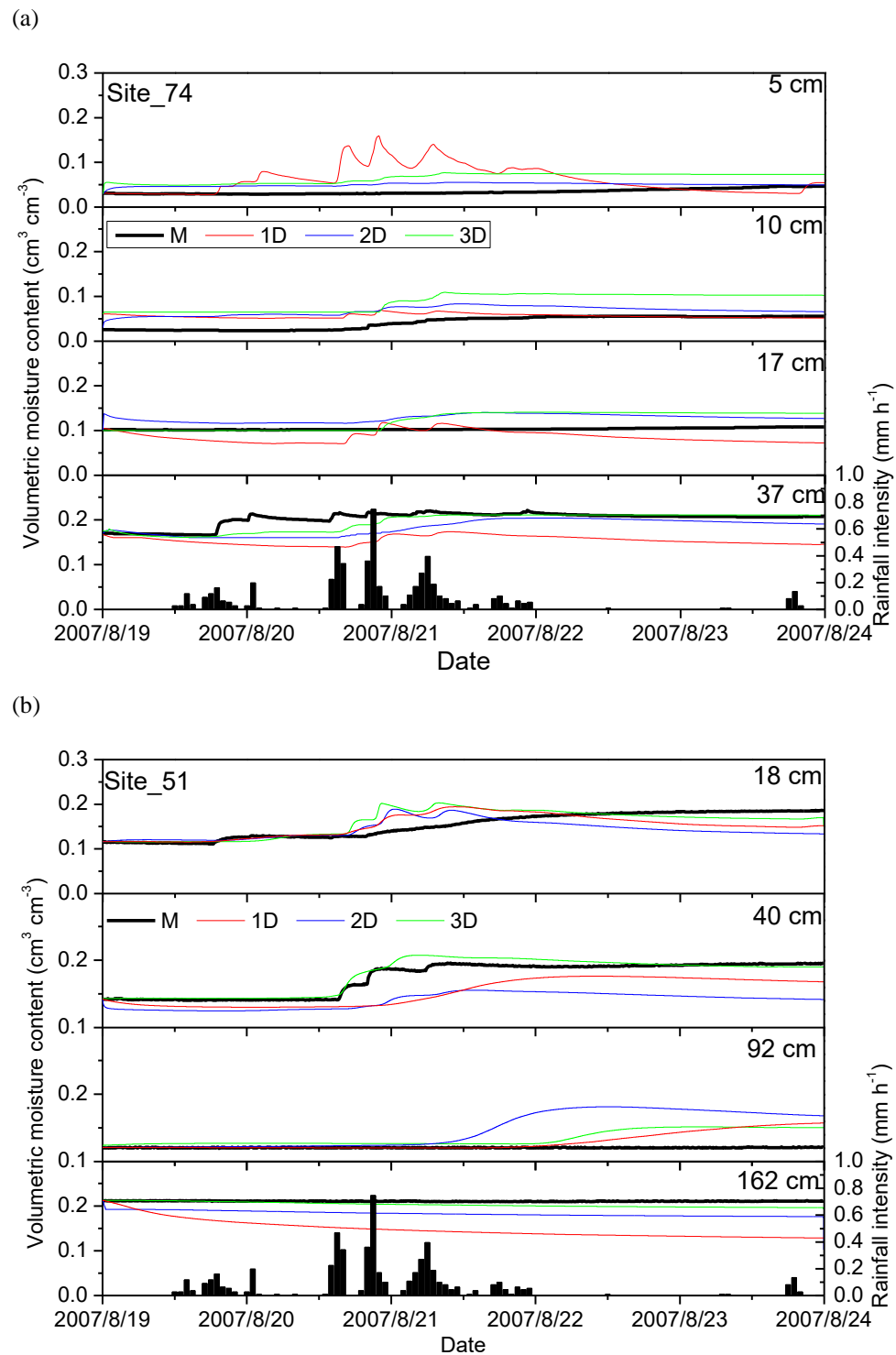
Figure 4. Measured (M) and predicted soil moisture values and rainfall intensities displayed over time during the drier period of August 19-24, 2007 at site_74 (a) and site_51 (b) by the HYDRUS-1D, -2D and -3D models.

(a)
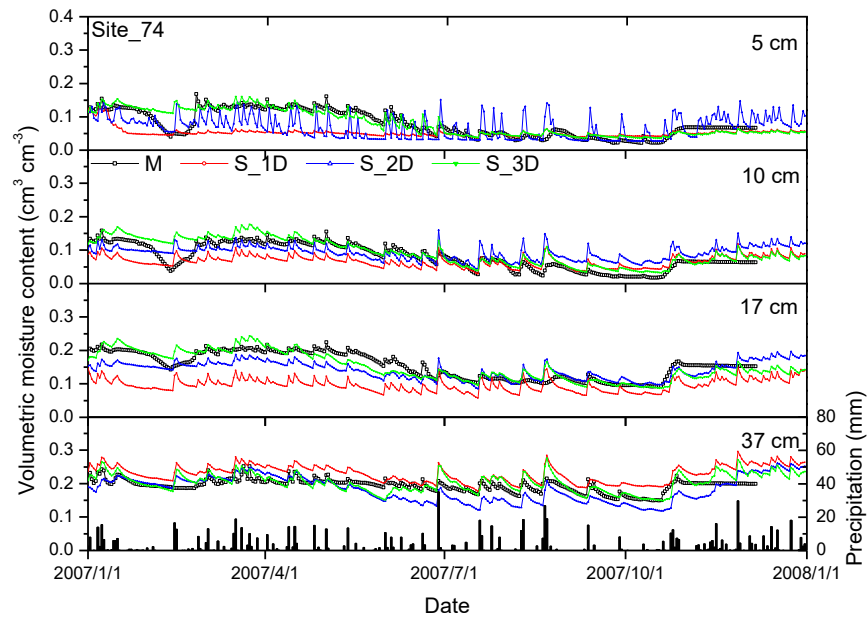
(b)
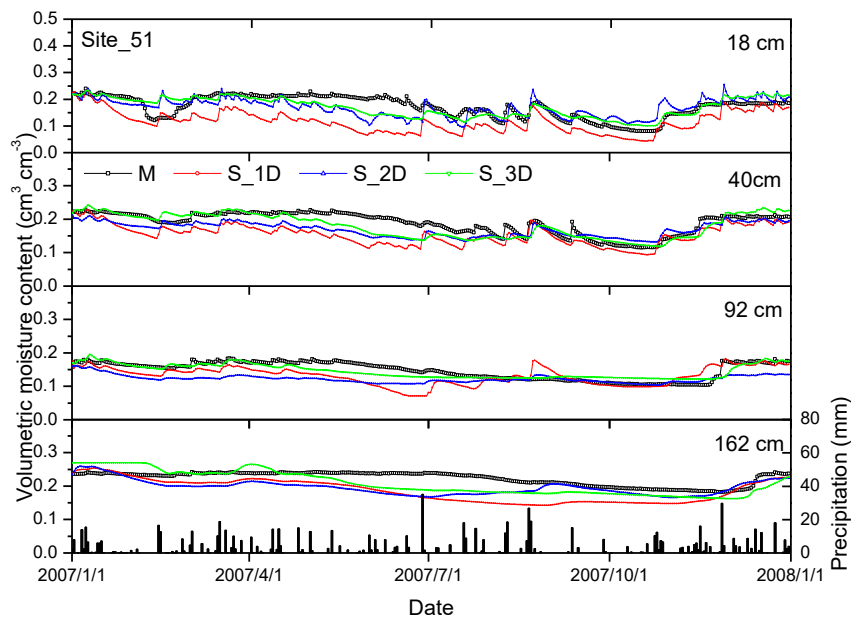
Figure 5. Measured (M) and predicted soil moisture values and rainfall intensities displayed over time in 2007 at site_74 (a) and Site_51 (b) by the HYDRUS-1D (S_1D), -2D (S_2D) and -3D (S_3D) models.
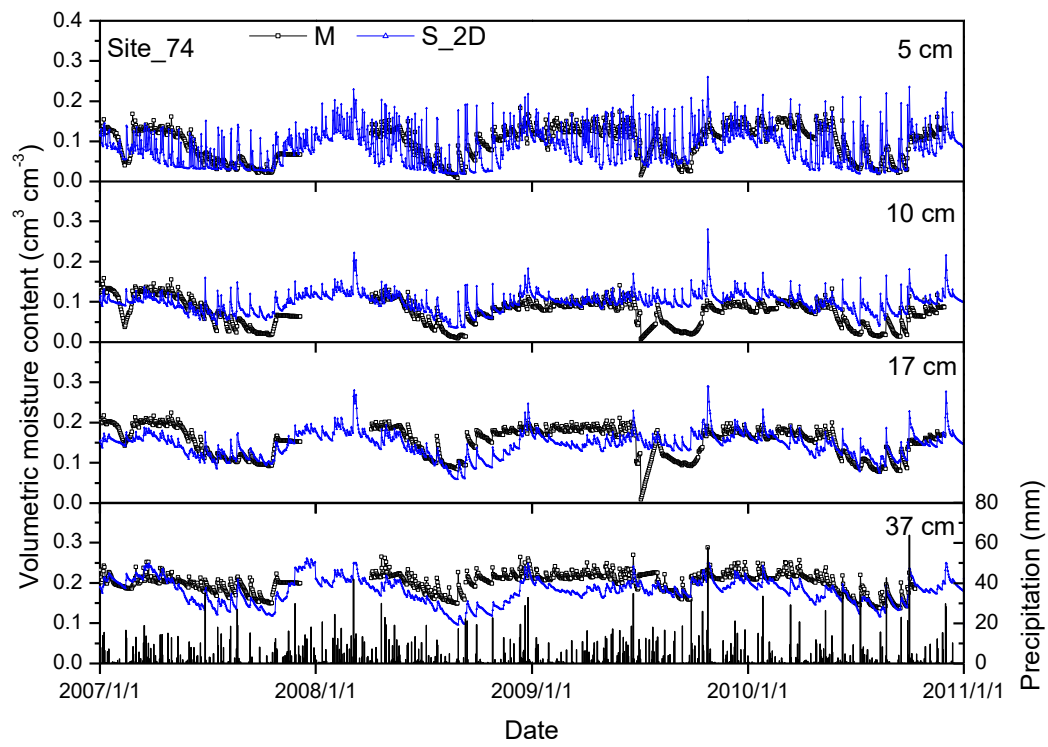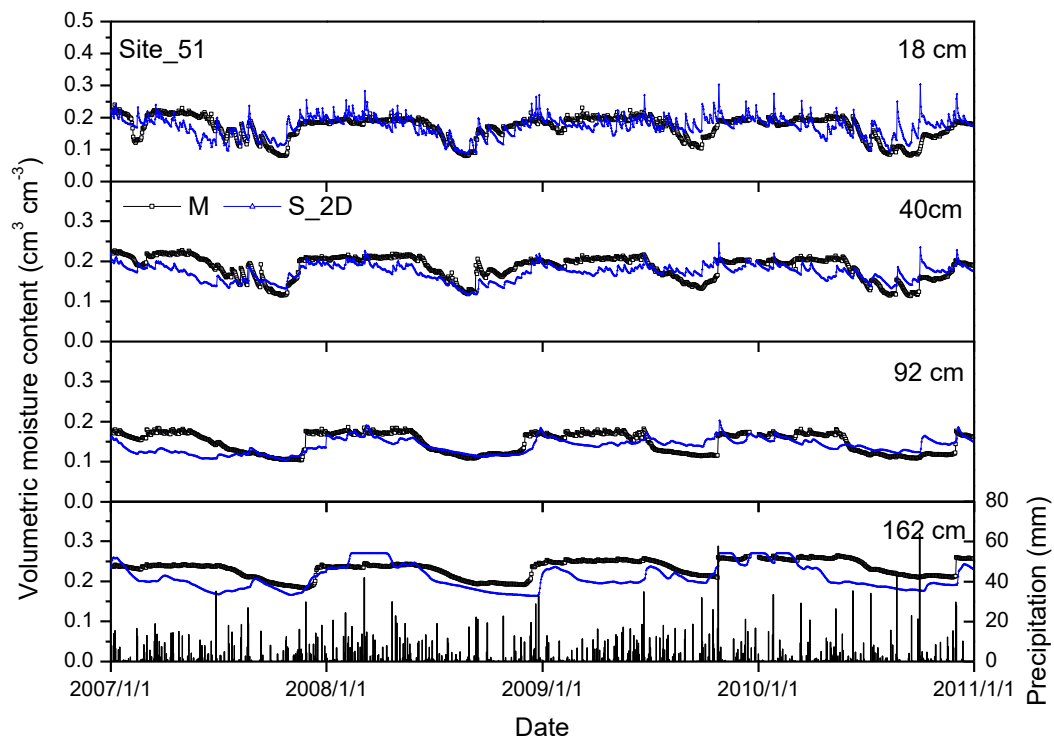
Figure 6. Measured (M) and predicted soil moisture values and rainfall intensities displayed over time in 2007-2010 for site_74 (a) and site_51 (b) by the HYDRUS- 2D model (S_2D).
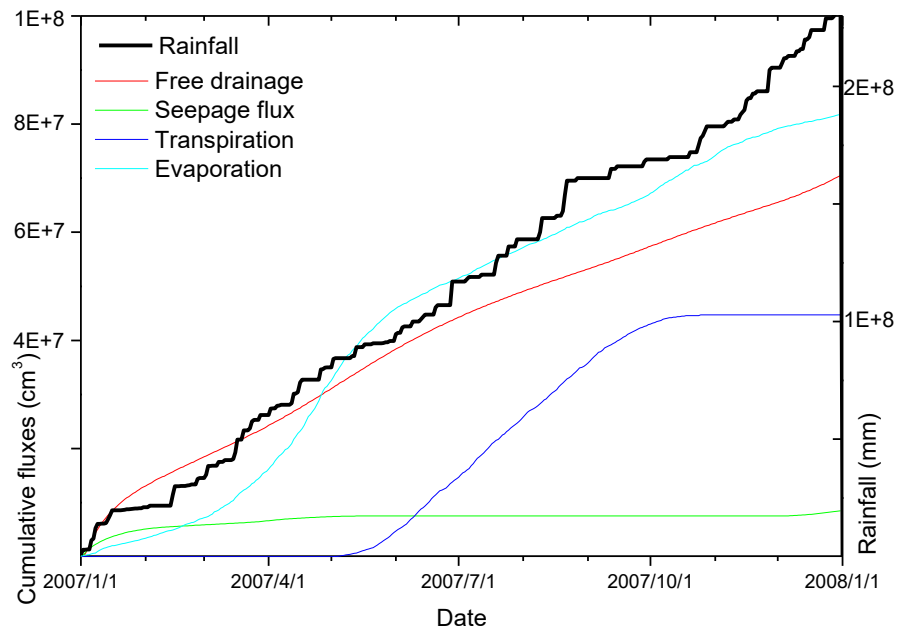
Figure 7. Cumulative fluxes of different terms of simulated water balances displayed over time for the studied area in 2007.
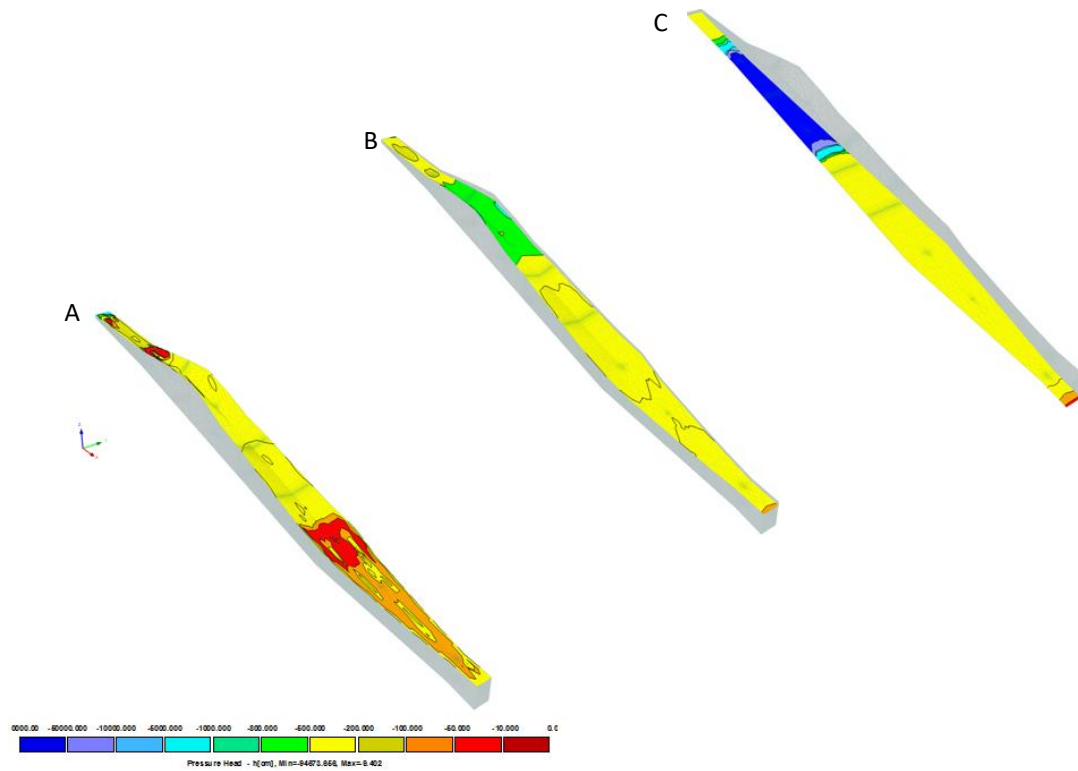
Figure 8. Snapshots of spatially variable pressure head at the 0-cm topsoil (A), the 40-cm subsoil (B), and the soil/bedrock interface (C) that were simulated by HYDRUS-3D for August 20, 2007.

(a)

(b)

Velocity

Velocity vectors
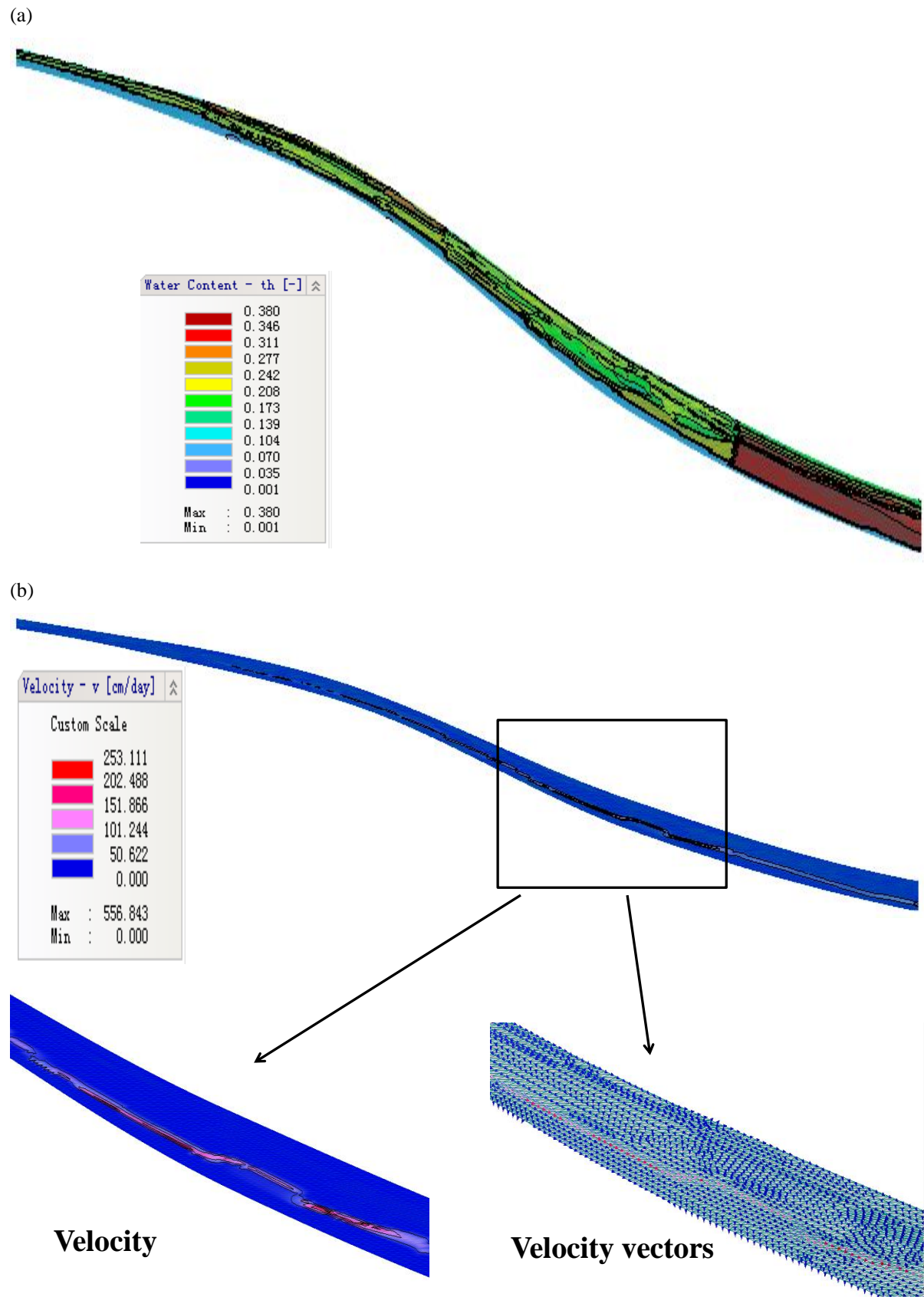
Figure 9. The 2D-distribution of (a) soil moisture content values and (b) water flux velocities displayed for August 20, 2007.

(a)
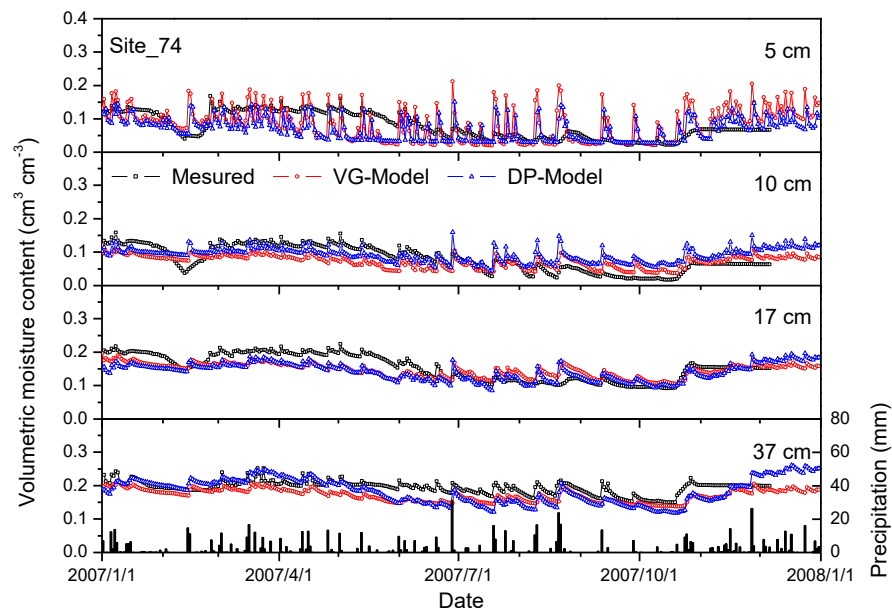
(b)
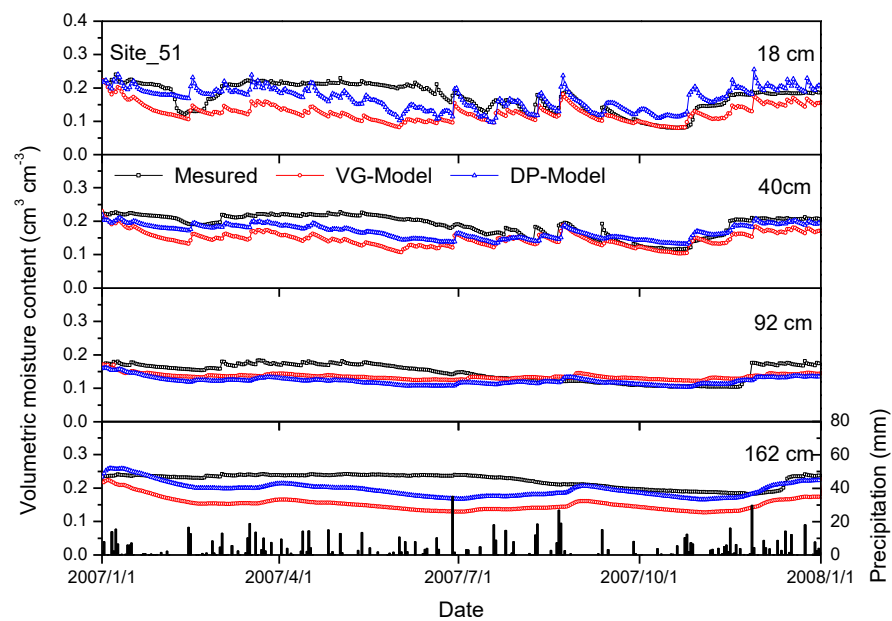
Figure 10. Comparisons between measured and predicted soil moisture values over time in 2007 for the single-porosity model (VG) and the dual-porosity model (DP) at site 74 (a) and site 51 (b) by the HYDRUS-2D model.

(a)
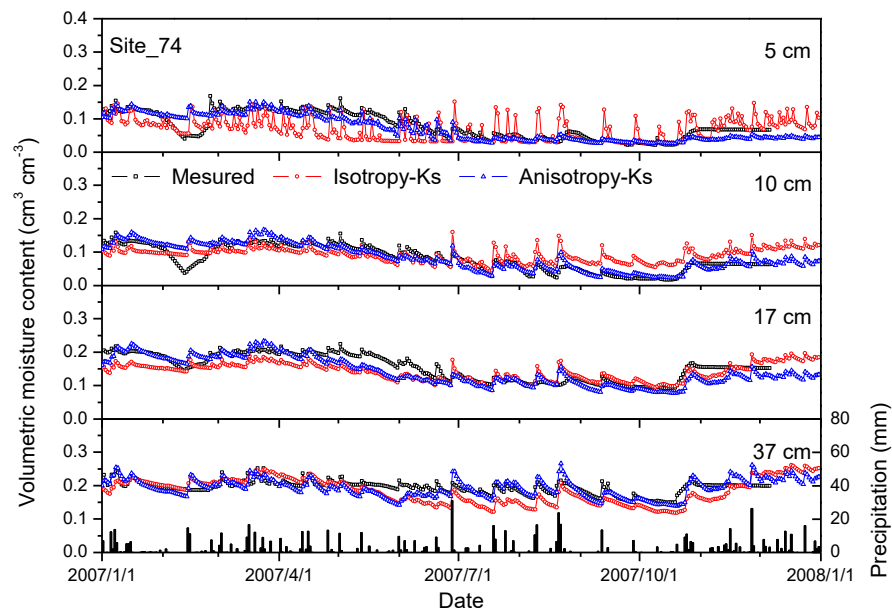
(b)
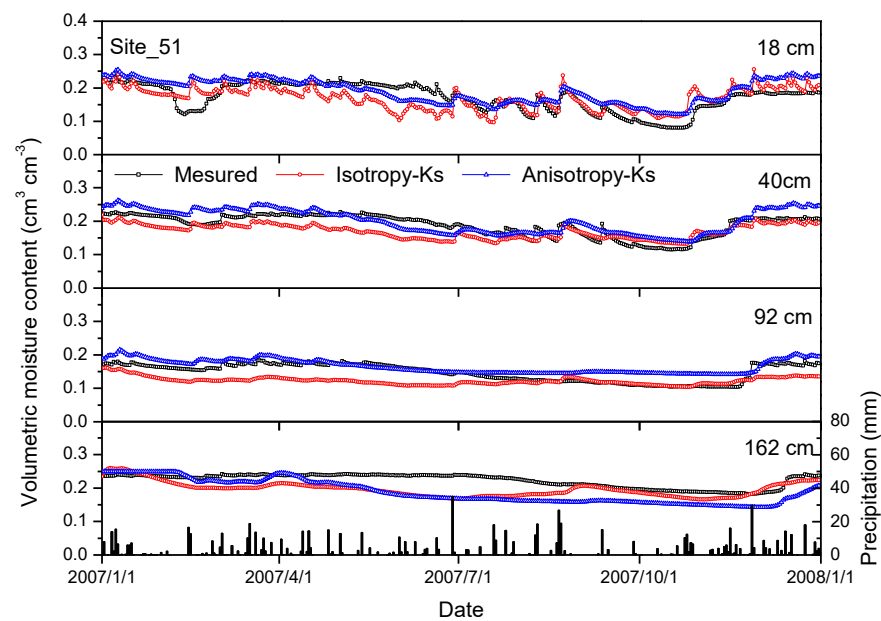
Figure 11. Comparisons between measured and predicted soil moisture values displayed over time in 2007 for isotropy-Ks and anisotropy-Ks at site 74 (a) and site 51 (b) by the HYDRUS-2D model.
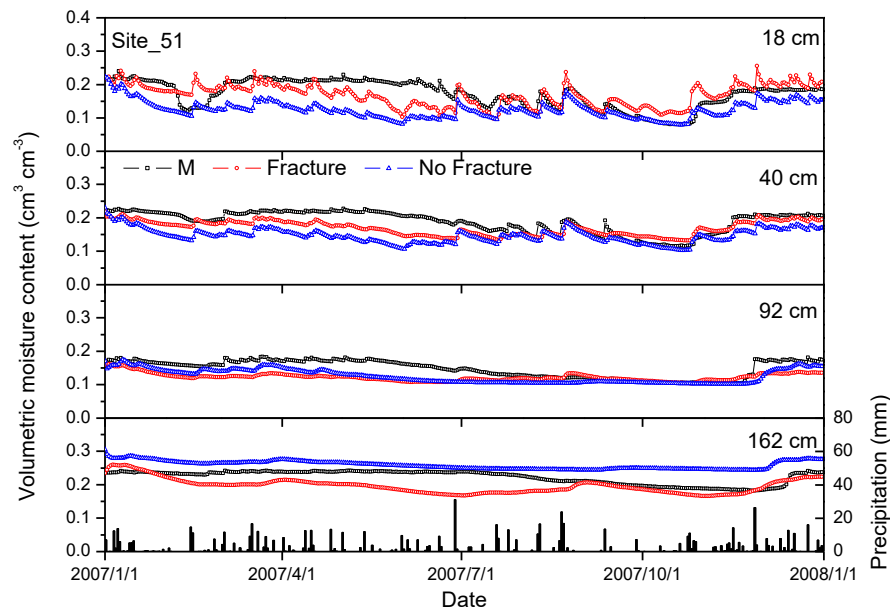
(a)
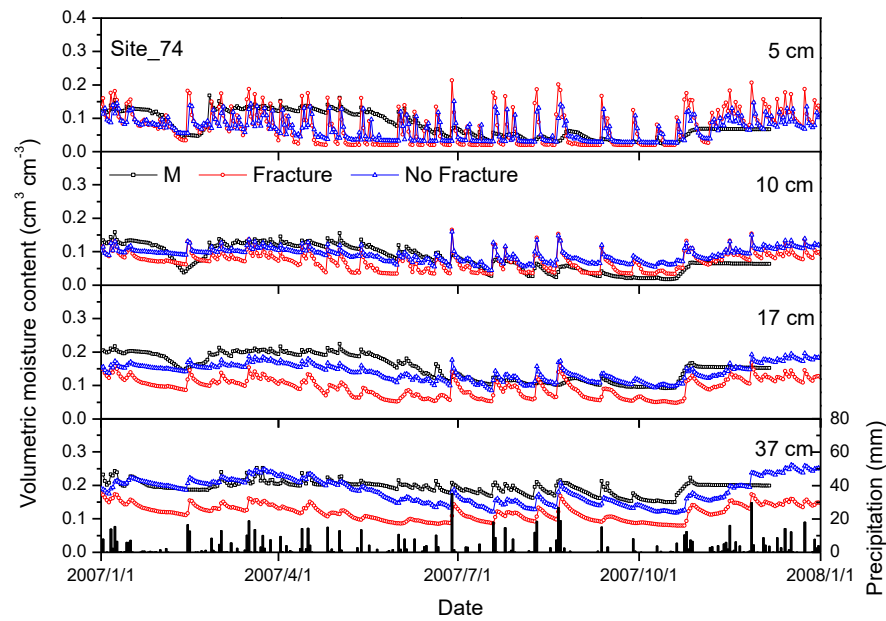
(b)

Figure 12. Comparisons between measured and predicted soil moisture values displayed over time in 2007 for permeable free drainage boundary condition (Fracture) and impermeable no-flux boundary condition (no fracture) for site 74 (a) and site 51 (b) by the HYDRUS-2D model.
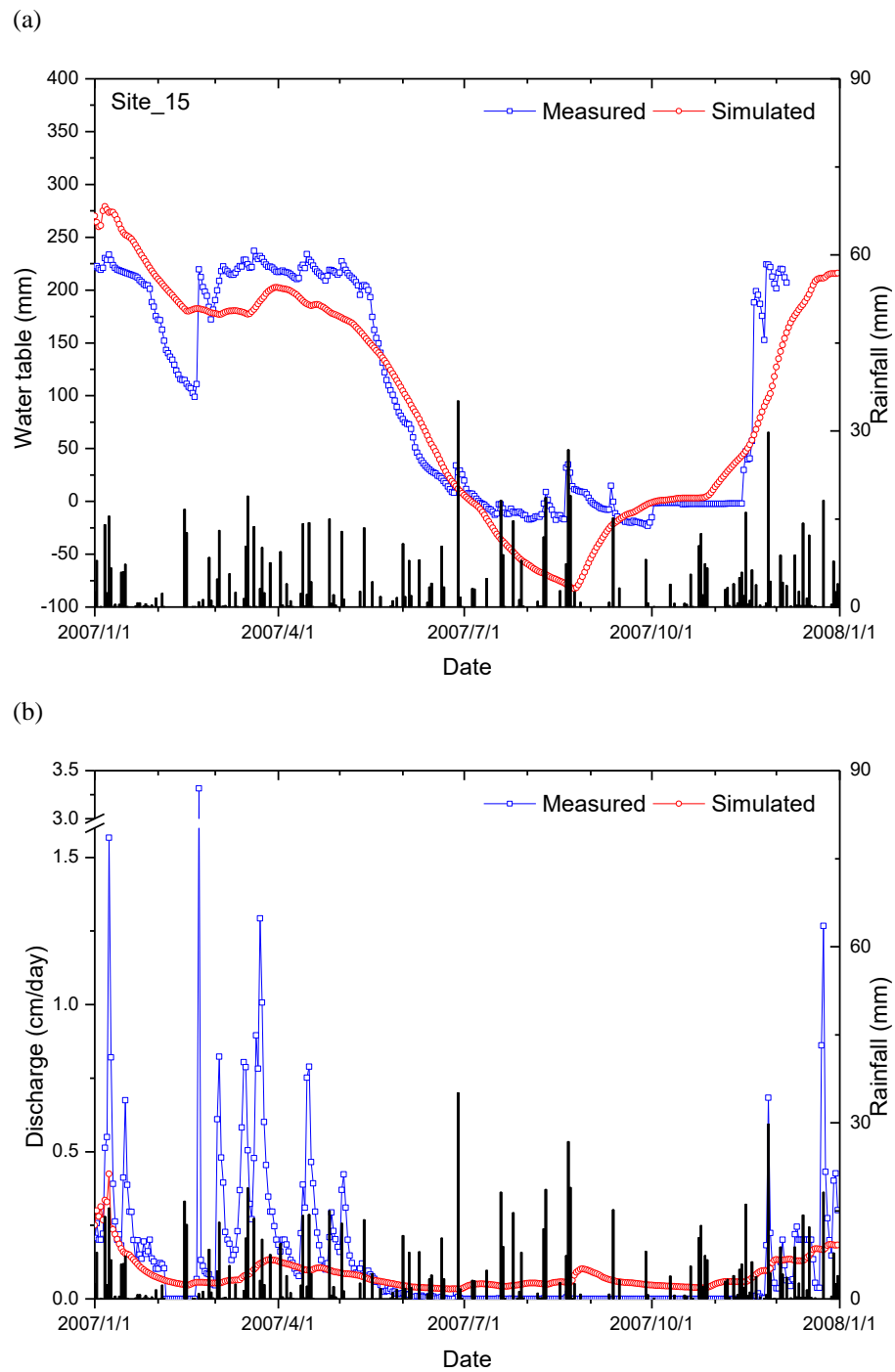
(a)

(b)

Figure 13. Comparisons between measured and simulated water tables for site 15 (a) and the measured discharge at the outlet of the catchment and simulated discharge for the sub-catchment evaluated during this study (b) with rainfall quantity distribution as a reference.
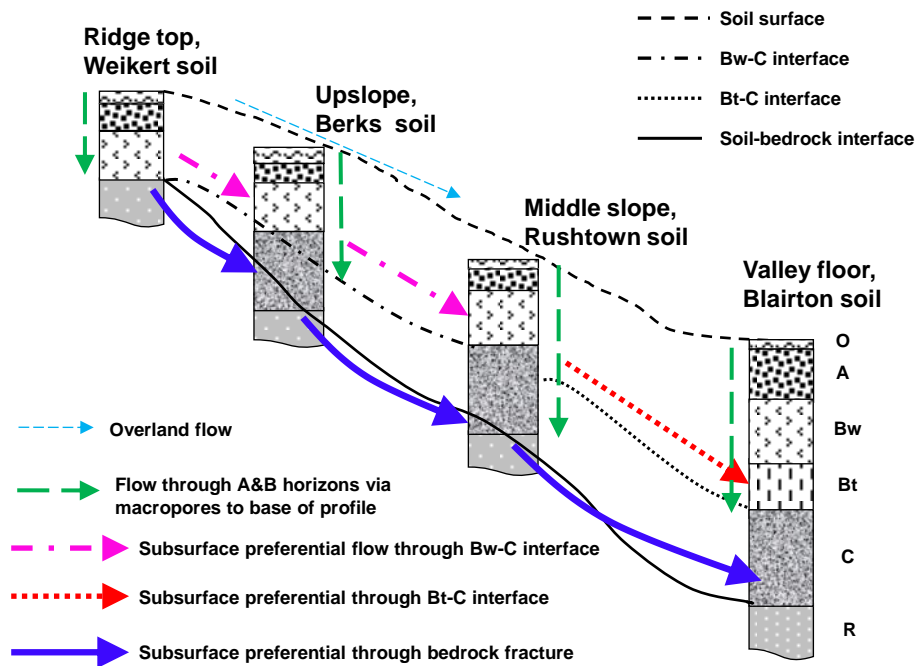
Figure 14. Conceptual diagram showing several potential subsurface preferential flow pathways along a hillslope in the Shale Hills catchment. The soil series and soil horizons are indicated for each landscape position, which is referenced in Table 1.